JACS
JOURNAL OF THE AMERICAN CHEMICAL SOCIETY
Article
Cite This: J. Am. Chem. Soc. 2018, 140, 14244−14266
pubs.acs.org/JACS

Dominant Role of Entropy in Stabilizing Sugar Isomerization Transition States within Hydrophobic Zeolite Pores

Michael J. Cordon,[†] James W. Harris,[†] Juan Carlos Vega-Vila,[†] Jason S. Bates,[†] Sukhdeep Kaur,[‡] Mohit Gupta,[‡] Megan E. Witzke,[§] Evan C. Wegener,[†] Jeffrey T. Miller,[†] David W. Flaherty,[§] David D. Hibbitts,[‡] and Rajamani Gounder*[,†]

[†]Charles D. Davidson School of Chemical Engineering, Purdue University, 480 Stadium Mall Drive, West Lafayette, Indiana 47907, United States

[‡]Department of Chemical Engineering, University of Florida, 1030 Center Drive, Gainesville, Florida 32611, United States

[§]Department of Chemical and Biomolecular Engineering, University of Illinois Urbana−Champaign, Urbana, Illinois 61801, United States

Supporting Information

ABSTRACT: Lewis acid sites in zeolites catalyze aqueous-phase sugar isomerization at higher turnover rates when confined within hydrophobic rather than within hydrophilic micropores; however, relative contributions of competitive water adsorption at active sites and preferential stabilization of isomerization transition states have remained unclear. Here, we employ a suite of experimental and theoretical techniques to elucidate the effects of coadsorbed water on glucose isomerization reaction coordinate free energy landscapes. Transmission IR spectra provide evidence that water forms extended hydrogen-bonding networks within hydrophilic but not hydrophobic micropores of Beta zeolites. Aqueous-phase glucose isomerization turnover rates measured on Ti-Beta zeolites transition from first-order to zero-order dependence on glucose thermodynamic activity, as Lewis acidic Ti sites transition from water-covered to glucose-covered, consistent with intermediates identified from modulation excitation spectroscopy during in situ attenuated total reflectance IR experiments. First-order and zero-order isomerization rate constants are systematically higher (by 3−12×, 368−383 K) when Ti sites are confined within hydrophobic micropores. Apparent activation enthalpies and entropies reveal that glucose and water competitive adsorption at Ti sites depend weakly on confining environment polarity, while Gibbs free energies of hydride-shift isomerization transition states are lower when confined within hydrophobic micropores. DFT calculations suggest that interactions between intraporous water and isomerization transition states increase effective transition state sizes through second-shell solvation spheres, reducing primary solvation sphere flexibility. These findings clarify the effects of hydrophobic pockets on the stability of coadsorbed water and isomerization transition states and suggest design strategies that modify micropore polarity to influence turnover rates in liquid water.

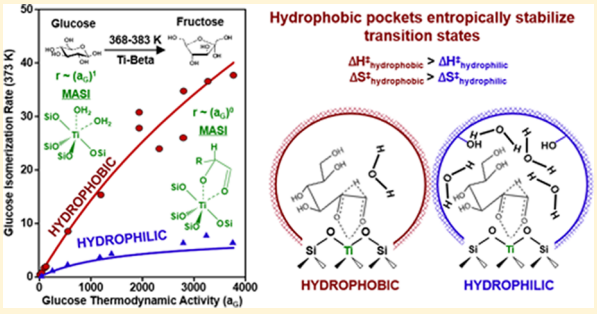

1. INTRODUCTION

Hydrophobic surfaces are characterized by weak hydrogen-bonding interactions with water molecules that cause structural changes to molecular ensembles and extended water networks near surfaces,[1] which are referred to collectively as "hydrophobic effects".[2] At least three distinct hydrophobic effects have been recognized during aqueous-phase reactions catalyzed within metalloenzymes, including hydrophobic side chains that provide contacts that increase free energies to drive water diffusion from binding pockets during protein folding,[3] hydrophilic side chains that hydrogen bond with water molecules to preferentially position them within specific locations in binding pockets,[4] and hydrophobic and hydrophilic groups that regulate water movement along reaction coordinates to facilitate enthalpy−entropy compromises that moderate reaction free energy landscapes.[5−7] Hydrophobic effects on water adsorption have also been observed at silica surfaces,[8] as well as within defect-free carbon nanotubes of subnanometer pore diameter[9] and defect-free silica surfaces positioned <1 nm apart,[10] which lack surface groups capable of hydrogen bonding and lead to the confinement of gaslike water rather than the "icelike" structures confined within highly defective and hydrophilic microporous voids. The influence of surrounding environment hydrophobicity on the structure and behavior of confined water has been noted generally in biomolecular recognition[2] and in reports of enhanced water transport in carbon nanotubes for separation and molecular-sensing applications,[11−14] in addition to applications in catalysis.[15,16]

Received: August 4, 2018
Published: September 28, 2018

DOI: 10.1021/jacs.8b08336
J. Am. Chem. Soc. 2018, 140, 14244−14266

Within the context of liquid-phase catalysis, hydrophobic pockets within inorganic microporous materials influence the free energies of reactive intermediates and transition states that result in differences in adsorption equilibrium constants and reaction rate constants. Several studies have focused on zeolites, which are crystalline silica-based materials whose microporous surfaces are composed of nonpolar and hydrophobic siloxane bonds, but these surfaces become increasingly hydrophilic with increasing densities of framework heteroatom substituents or of silanol and other hydroxyl groups that donate and accept hydrogen bonds.[17−20] Silanol groups originate from framework siloxy (i.e., SiO^-) defects that form during hydrothermal synthesis when cationic structure-directing agents are not charge-balanced either by aliovalent heteroatoms substituted in framework positions (e.g., Al^{3+})[21,22] or by counteranions occluded within extraframework locations (i.e., F^-).[23−25] Silanol groups can also form after synthesis upon hydrolysis of framework siloxane linkages in neutral or basic aqueous media,[26,27] or upon removal of framework heteroatoms (e.g., Al, B) in acidic media.[28,29] The adsorption of gaseous water on zeolites measured by gravimetry increases with silanol density,[30,31] consistent with higher intraporous water densities that are stabilized with increasing silanol density when zeolites are contacted or equilibrated with liquid water.[32] Higher intraporous water densities have been shown to influence the kinetics of catalytic reactions, such as to cause preferential stabilization of protonated water and propanol clusters during gas-phase propanol dehydration on Brønsted acidic Al-MFI zeolites that enhances rates of bimolecular or trimolecular dehydration pathways over those of monomolecular routes.[33] Hydrophobic channels in Lewis acidic Ti-MFI zeolites increase 1-hexene epoxidation rates relative to hydrophilic TiO_2−SiO_2 surfaces by mitigating the formation of bulk water structures near Ti sites,[34] while silanol groups near Ti sites in UCB-4 zeotypes lead to increases in cyclohexene epoxidation rates.[35] Hydrophobic channels also increase rates for a variety of monomolecular and bimolecular reactions, such as aqueous-phase and biphasic *m*-cresol alkylation with 2-propanol in Al-FAU zeolites,[36,37] aqueous-phase 1-hexene epoxidation on Ti-MWW zeolites,[38] hydrogenation and etherification of hydroxymethylfurfural in alcohol solvents on metal-substituted Beta zeolites,[39] gas-phase bimolecular ethanol dehydration at high water partial pressures on Sn-Beta zeolites,[40,41] and aqueous-phase Meerwein−Ponndorf−Verley reduction and Oppenauer oxidation (MPVO) reactions in Ti-Beta[42] and Sn-Beta zeolites.[32]

Here, we study aqueous-phase glucose isomerization catalysis that proceeds via Lewis acid-mediated intramolecular hydride shift steps on a suite of materials synthesized with site-isolated framework Ti centers (Si/Ti = 30−300) and residual silanol defect densities that vary by 2 orders of magnitude (10^{-5}−10^{-3} mol g^{-1}) to isolate the kinetic effects of hydrophobic confining pockets around Ti centers. In prior reports, first-order aqueous-phase glucose isomerization rate constants were higher on hydrophobic Ti-Beta (∼7−10×, 373 K)[42] and Sn-Beta (∼50×, 373 K)[32] zeolites than their hydrophilic analogues, but rate data measured in first-order kinetic regimes are unable to resolve the kinetic contributions of glucose and water competitive adsorption from those of isomerization transition state stabilization. Coadsorbed water within Sn-Beta micropores has been reported to decrease experimentally measured glucose and 1,3-dihydroxyacetone isomerization rates, which was attributed to the competitive adsorption of water and substrate molecules at Sn sites.[43] In contrast, density functional theory (DFT) studies report that silanol defects in Sn-Beta lower activation barriers to form 1,2-hydride shift transition states during glucose−fructose isomerization[44] and enthalpically stabilize adsorbed deprotonated glucose intermediates[45] via hydrogen-bonding interactions, while ab initio molecular dynamics (AIMD) simulations indicate that explicit coadsorbed water molecules lower activation free energies via solvent reorganization and charge redistribution throughout the reaction coordinate.[46] These studies emphasize that understanding the specific structure and density of coadsorbed water molecules under reaction conditions, and their separate influence on the free energies of reactive intermediates and transition states involved in sugar isomerization, remains a relevant and active area of research.

The incomplete understanding of water density and structure within microporous environments of different polarity precludes more precise definitions of the kinetic and mechanistic effects of hydrophobic reaction pockets on sugar isomerization catalysts. Here, we report a detailed kinetic analysis of initial glucose isomerization turnover rates (normalized per Lewis acid site) on hydrophobic Ti-Beta-F and hydrophilic Ti-Beta-OH zeolites in first-order and zero-order kinetic regimes as a function of temperature (368−383 K), which enables measuring rate constants, activation enthalpies, and activation entropies that separate the effects of confining environment polarity on transition state stabilization and water competitive adsorption. The kinetic effects of coadsorbed solvent molecules on relevant intermediates and transition states are determined from a suite of ex situ and in situ experimental characterizations and insights from DFT calculations. These combined experimental and computational results highlight the dominant role of hydrophobic pockets to prevent the formation of extended water structures. Such coadsorbed water structures confer modest enthalpic stabilization, but more severe entropic destabilization, of isomerization transition states that ultimately lead to lower turnover rates.

2. MATERIALS AND METHODS

2.1. Catalyst Synthesis. Ti-Beta-F zeolites were synthesized in fluoride media following a previously reported hydrothermal synthesis method.[30] Gels were prepared by first mixing 4.89 g of tetraethylammonium fluoride (TEAF, Alfa Aesar, 97 wt %) with 7.25 g of deionized water (18.2 MΩ) in a perfluoroalkoxy alkane (PFA) container (Savillex Corp.) followed by the addition of 10.0 g of tetraethylorthosilicate (TEOS, Sigma-Aldrich, >98 wt %). The resulting gel was stirred for 1 h prior to adding 0.221 g of titanium(IV) isopropoxide (TIPO, Sigma-Aldrich, 99.999%). The PFA container was sealed and the contents stirred for 16 h prior to removing the cover to allow ethanol, isopropanol, and excess water to evaporate. The final gel molar composition was 1 SiO_2/*x* TIPO/0.55 TEAF/7.15 H_2O, where *x* ranged between 0.005 and 0.0087. The gel was then loaded and sealed into a Teflon-lined stainless steel autoclave (45 cm^3, Parr Instruments) with 0.14 g of Si-Beta-F (∼5% of Si in the gel) and heated to 413 K while rotating (60 rpm) in an isothermal oven (Yamato DKN-402C) for 25 d. The products were removed from the liner and washed with water and acetone (Sigma-Aldrich, >99.5 wt %, 6 washes each, ∼20 cm^3 (g zeolite)$^{-1}$ per wash), centrifuged to recover the solid portion, and dried for 16 h at 373 K. The resulting solids were then heated in a muffle furnace (Nabertherm LE 6-11 with P300 controller) in flowing dry air (Indiana Oxygen, Ultra Zero grade, 1.67 cm^3 s^{-1} (g solids)$^{-1}$) to 853 K (0.0167 K s^{-1}) for 10 h.

DOI: 10.1021/jacs.8b08336
J. Am. Chem. Soc. 2018, 140, 14244−14266

Ti-Beta-OH zeolites were prepared using a previously reported post-synthetic reflux technique.[47] Briefly, Al-Beta zeolites (Si/Al = 20−50) were synthesized using a method similar to that reported previously[48] without the aluminosilicate gel filtration step. The recovered solids were washed, centrifuged, dried, and treated in air, as described above for Ti-Beta-F preparation. The resulting Al-Beta samples were dealuminated by stirring with nitric acid (69 wt % HNO_3, Avantor, 25 cm^3 of solution per 1 g of H-form zeolite) in a covered PFA container for 16 h at 353 K. The solids were then washed thoroughly with water until a constant supernatant pH was observed, isolated via centrifugation, and dried for 16 h at 373 K. Dealuminated Beta samples were then treated in flowing dry air (Indiana Oxygen, Ultra Zero grade, 1.67 $cm^3\ s^{-1}$ (g solids)$^{-1}$) to 853 K (0.0167 K s^{-1}) for 10 h. On each dealuminated Beta sample, the resulting Si/Al ratio was >1500 as measured by atomic absorption spectroscopy (AAS). Afterward, 2 g of dealuminated Beta were loaded into a 500 cm^3 round-bottom flask and dried for 12 h on a Schlenk line under rough vacuum (Oerlikon Trivac 140002E2, ∼0.04 Torr). Dichloromethane (CH_2Cl_2, Sigma-Aldrich, >99.8%) was dried over 3A molecular sieves (W. R. Grace, 4−8 mesh, grade 562) prior to being transferred via moisture-free and air-free cannula to the flask containing the dealuminated Beta zeolites. A solution of titanium(IV) tetrachloride predissolved in CH_2Cl_2 (Sigma-Aldrich, 1.0 M $TiCl_4$ in CH_2Cl_2) was further diluted in dry CH_2Cl_2 to achieve a concentration of 1 mmol $TiCl_4$/g of dealuminated Beta prior to cannula transfer to the round-bottom flask containing the dealuminated zeolite sample. This mixture was heated for 7 h under reflux at 333 K. The solids were then collected via centrifugation, washed 6 times (∼60 cm^3 per wash) with methanol (Sigma-Aldrich, >99.9%), dried for 16 h at 373 K, and then thermally treated in air (Indiana Oxygen, Ultra Zero grade, 1.67 $cm^3\ s^{-1}$ (g solids)$^{-1}$) to 473 K (0.05 K s^{-1}) for 6 h and then at 823 K (0.05 K s^{-1}) for 6 h in a muffle furnace.

2.2. Characterization of Bulk Catalyst Properties. Bulk elemental compositions were determined using AAS on a PerkinElmer AAnalyst 300 Atomic Absorption spectrometer after calibration using standard solutions for each element generated by dilution of 1000 ppm AAS standards (Alfa Aesar, TraceCERT, ±4 ppm). Typically, 0.02 g of zeolite samples were dissolved in 2.6 g of HF (48 wt %, Alfa Aesar) and 50 g of deionized water prior to characterization. Extreme caution should be taken when working with hydrofluoric acid, and appropriate personal protective equipment, ventilation, and other engineering controls should be used. Absorbance values were measured in an acetylene/nitrous oxide flame at 396.2, 399.9, and 251.6 nm for Al, Ti, and Si, respectively. Samples are denoted as Ti-Beta-X-Y, where X refers to the synthetic history (F = fluoride-mediated hydrothermal synthesis; OH = post-synthetic grafting of dealuminated Al-Beta) and Y reflects the bulk Si/Ti ratio (by AAS).

Powder X-ray diffraction (XRD) patterns were collected using a Rigaku Smartlab X-ray diffractometer with a Cu Kα source (1.76 kW) and an ASC-6 automated sample changer. Zero-background, low-dead-volume sample holders (Rigaku) were loaded with ∼0.01 g of sample prior to collecting diffraction patterns from 4 to 40° at a scan rate of 0.00417° s^{-1} with a step size of 0.01°. The presence of TiO_x domains larger than 3 nm (25.4° and 37.9° for anatase, 27.4° and 35.2° for rutile) was not observable in the XRD pattern of any sample studied here.

Nitrogen (77 K), water (293 or 298 K), and methanol (293 K) adsorption isotherms were collected using a Micromeritics ASAP2020 Surface Area and Porosity analyzer. Typically, ∼0.03 g of sample were pelleted and sieved to obtain particle diameters between 180 and 250 μm. Samples were degassed prior to analysis by heating to 393 K (0.0167 K s^{-1}) under vacuum (<0.005 Torr) for 2 h then heating to 623 K (0.0167 K s^{-1}) under vacuum for 8 h. A semilog derivative analysis of N_2 isotherms ($\delta(V_{ads}/g)/\delta(\log(P/P_0)$ vs log (P/P_0)) was used to identify the end of the micropore filling regime, in order to quantify the micropore volume of each sample. Water uptakes are reported at a reduced pressure of 0.2, which has been used previously[49] as a reference pressure corresponding to micropore filling of cyclohexane (298 K) within hydrophobic zeolites.

Scanning electron microscopy (SEM) was performed on a FEI Quanta 3D FEG Dual-beam SEM equipped with an Everhart-Thornlev detector for high-vacuum imaging. The focused beam operating mode was used to collect SEM micrographs with a spot size of 4 μm and a voltage of 5 kV.

Diffuse reflectance UV−vis (DRUV) spectra were collected on a Varian Cary 5000 UV−vis−NIR equipped with a Harrick Praying Mantis in situ diffuse reflectance cell. UV−vis spectra were collected at ambient conditions prior to thermally treating samples to 523 K (1800 s, ∼0.5 K s^{-1}) in dry flowing He (4.17 $cm^3\ s^{-1}$ (g solids)$^{-1}$), at which point spectra of dehydrated samples were collected at 523 K. Spectra were collected at a resolution of 10 nm s^{-1} using poly(tetrafluoroethylene) (PTFE, Sigma-Aldrich, 1 μm powder) as the 100% reflectance standard. Diffuse reflectance spectra were converted into absorbance spectra using the Kubelka−Munk (F(R)) function. Band centers are reported as that corresponding to the highest F(R) intensity on dehydrated samples.

2.3. Transmission Infrared Spectroscopy. A Nicolet 4700 spectrometer with a Hg−Cd−Te detector (MCT, cooled to 77 K by liquid N_2) was used to collect IR spectra by averaging 64 scans at a resolution of 2 cm^{-1} in the 4000 to 400 cm^{-1} range. Spectra were taken relative to an empty cell background reference collected under dynamic vacuum (<0.1 Torr, rotary vane rough pump, Alcatel 2008A) at either 303 K for deuterated acetonitrile (CD_3CN) adsorption studies or 423 K for pyridine adsorption studies. Self-supporting wafers of 0.01−0.03 g cm^{-2} were sealed in a custom-built quartz IR cell[50] with CaF_2 windows positioned within an alumina silicate ceramic chamber (Purdue Research Machining Services) with a mineral-insulated resistive heating coil (ARi Industries). K-type thermocouples (Omega) were positioned within 2 mm of each side of the wafer. A custom glass vacuum manifold was used for sample pretreatment and for dosing controlled amounts of gaseous titrants into the cell. Wafers were first thermally treated to 823 K (0.083 K s^{-1}) for 1 h in flowing dry air (6.66 $cm^3\ s^{-1}$ (g solids)$^{-1}$), which was further purified by a Fourier transform infrared (FTIR) purge gas generator (<1 ppm of CO_2, 200 K water dew point, Parker Balston) prior to each experiment. Wafers were then exposed to dynamic vacuum for 1 h at 823 K (<0.1 Torr, rotary vane rough pump, Alcatel 2008A).

For CD_3CN titration experiments, wafers were then cooled under dynamic vacuum to 303 K. CD_3CN (Sigma-Aldrich, >99.9%, 99.96 atom % D) was purified through three freeze−pump−thaw cycles prior to dosing ∼1.5×10^{-7} mol into the cell (similar procedures for pyridine titration given in Section S.1.2, Supporting Information). The cell was allowed to equilibrate for 180 s at a constant final pressure for each dose prior to collecting each IR spectrum. Subsequent doses were introduced until wafer saturation was achieved, which was determined when final pressures > 0.4 Torr were observed due to residual gaseous titrant within the cell. Wafers were then exposed to dynamic vacuum at the dosing temperature to remove gas-phase and weakly adsorbed species until a final pressure of 0.0 Torr was measured in the cell. IR spectra were baseline-corrected and normalized to combination and overtone modes of zeolite Si−O−Si stretches (1750−2100 cm^{-1}) followed by subtraction of the parent spectrum and deconvolution of the CD_3CN IR peaks into their individual components (2308, 2275, and 2265 cm^{-1}) as reported elsewhere.[32] Peak areas were used in conjunction with integrated molar extinction coefficients (E) to determine site concentrations per gram of zeolite:

$$\text{site density } (\mu\text{mol g}^{-1}) = \left(\frac{\text{peak area } (\text{cm}^{-1})}{E\ (\text{cm } \mu\text{mol}^{-1})}\right) \times \left(\frac{a_{CS}\ (\text{cm}^2)}{m\ (\text{g})}\right) \quad (1)$$

In the case of CD_3CN adsorbed onto silanol groups (2275 cm^{-1}), an integrated molar extinction coefficient value (E (2275 cm^{-1}) = 0.74 cm μmol^{-1}) measured on dealuminated Beta was used.[32] In the case of Lewis acidic Ti sites that give rise to the CD_3CN IR peak at 2308 cm^{-1}, an integrated molar extinction coefficient was measured following previously reported methods.[32] Briefly, Ti-Beta wafers were

DOI: 10.1021/jacs.8b08336
J. Am. Chem. Soc. 2018, 140, 14244−14266

pretreated as mentioned earlier and sequentially dosed with small amounts of CD_3CN in vacuum (0.1−0.3 μmol of CD_3CN per dose) prior to equilibration for 180 s. For these initial doses, the final recorded pressure in the cell was measured to be 0.0 Torr, and all of the CD_3CN dosed into the cell was assumed to be adsorbed onto the sample wafer. IR spectra were collected after each dose, baseline-corrected and normalized, and then deconvoluted into constituent peaks associated with $\nu(C{\equiv}N)$ stretching vibrations for CD_3CN adsorbed onto Lewis acidic Ti sites (2308 cm^{-1}) and silanols (2275 cm^{-1}) and for gas-phase or physisorbed CD_3CN (2265 cm^{-1}) at higher doses. The number of CD_3CN adsorbed onto Lewis acidic Ti sites was determined by quantifying the total amount of adsorbed CD_3CN via equilibrated pressure differences before and after dosing and subtracting contributions from silanol-bound CD_3CN.

For water adsorption experiments, the cell was first assembled without a sample wafer to quantify the contributions of water in the gas phase and adsorbed on cell windows. The cell was treated in flowing He (UHP, Indiana Oxygen, 0.96 $cm^3\ s^{-1}$) at 823 K (0.0833 K s^{-1}) for 1 h, then cooled to 298 K. The temperature was controlled at 298 K (±2 K, the gradient observed between the two thermocouples on either side of the wafer was <1.5 K) by flowing air free of carbon dioxide and moisture through the cooling channels of the insulated brass block and by resistive heating. A spectrum was collected at 298 K in flowing He (0.96 $cm^3\ s^{-1}$) and used as the background for all subsequent spectra. Liquid water (18.2 MΩ) was vaporized into the flowing He stream (0.96 $cm^3\ s^{-1}$) from a syringe pump (KD Scientific Legato 100) equipped with a 1 cm^3 syringe (Hamilton) and delivered to the cell in heated lines (>363 K). The liquid water flow rate was varied to achieve partial pressures of 0.32, 0.63, 1.58, and 2.37 kPa, corresponding to P/P_0 = 0.10, 0.20, 0.50, and 0.75, respectively, at 298 K. Spectra were averaged over 64 scans at 2 cm^{-1} resolution in the 4000−650 cm^{-1} range and were monitored over time at each condition until invariant (>1800 s), indicating that equilibrium was reached. After equilibrium was verified, a 640-scan spectrum at 2 cm^{-1} resolution was collected to average out temporal variations in gas-phase pressures and temperature.

Next, self-supporting wafers (0.015−0.040 g) of Ti-Beta-F-155 and Ti-Beta-OH-46 were pressed and loaded into the cell and subjected to treatments identical to those described earlier for the empty cell. Spectra were processed first to remove the contributions of water adsorbed in the cell and gas-phase water by subtracting the respective spectrum of the empty cell measured at the same P/P_0 value. Then, spectra were normalized by the combination and overtone modes of zeolite Si−O−Si stretches (1750−2100 cm^{-1}) of the wafer prior to water exposure followed by subtraction of the normalized spectrum for the sample before water adsorption. The resulting difference spectra represent the vibrations of adsorbed water and any differences on the sample induced by this adsorption (e.g., perturbation of silanol groups). These spectra were further baseline-corrected with pivot points at 4000, 2400, and 1350 cm^{-1}, where no absorbance was detected.

2.4. Glucose Isomerization Kinetic Studies. Kinetic studies were performed in 10 cm^3 thick-walled glass batch reactors (VWR) with 1−50 wt % aqueous D-glucose (Sigma-Aldrich, ≥99.5%) solutions. The reactant solutions were first prepared by adjusting the pH of deionized water (18.2 MΩ) with hydrochloric acid (HCl, Macron, 37 wt %) to 4 for kinetic studies performed at ≤373 K or 3 for kinetic studies performed at >373 K, in order to suppress contributions from background isomerization reactivity catalyzed by hydroxide anions. The pH-adjusted water was then mixed with D-glucose to the desired concentration, filtered (0.2 μm PTFE filters, VWR), and loaded into 2 mL glass vials capped with a PTFE/silicone septum (Waters) for preheating. Catalytic solids (~0.01−0.06 g) were added to a batch reactor and sealed with a crimp top (PTFE/silicone septum, Agilent). The vials containing the reactant solution and the catalyst were heated separately for 600 s to the reaction temperature atop a digital stirred hot plate (IKA RCT basic) prior to injecting ~1−4 cm^3 of the preheated reactant solution into the capped reactors.

Reactors were maintained at temperature (368−383 K, 750 rpm, autogenous pressure) for various time intervals (300−14 400 s) before quenching in an ice bath. Product solutions were filtered (0.2 μm, PTFE), diluted to 1 wt % sugar concentration with deionized water, and then mixed with a 1 wt % aqueous D-mannitol (Sigma-Aldrich, ≥98 wt %) solution as an internal quantification standard. Product separation was performed using an Agilent 1260 high-performance liquid chromatograph (HPLC) with an aqueous mobile phase (0.01 $cm^3\ s^{-1}$, 353 K) through a Hi-Plex Ca column (7.7 × 300 mm, 8 μm particle size, Agilent). Quantification was performed using an Agilent 1260 Infinity evaporative light-scattering detector (ELSD) using separate calibration curves for each sugar compound. Initial rates were determined by extrapolating transient product formation rates to zero reaction time, a procedure that gave values identical to rate measurements from batch reactors operated at differential conversions (<5%) upon correcting for approach to equilibrium. Reaction enthalpies and entropies were obtained from Bayesian nonlinear regression in Athena Visual Studio (Athena Visual Software, Inc., version 14.2), and reported errors represent 95% marginal highest posterior density intervals.

Isotopic labeling studies were performed using 1 cm^3 of a 5 wt % aqueous D-glucose-D_2 (Cambridge Isotope Laboratories, 98% 2-D) solution (pH = 4) and 0.01−0.04 g of catalytic solids for variable times (300−3600 s) at 373 K. Reactor contents were then quenched, and products were filtered and separated as described earlier. Liquid samples containing products and unreacted glucose were collected using an Agilent 1260 Infinity series fraction collector, frozen in liquid N_2 to 77 K, and freeze-dried to remove water using a Labconco FreeZone lyophilizer (<0.01 Torr, 36 h). Afterward, 0.06 cm^3 D_2O (Cambridge Isotope Laboratories, 99.9%) was added to dissolve dried sugar products prior to loading into NMR tubes (Wilmad LabGlass, 5 mm thin wall, 7 in., 500 MHz) for liquid NMR analysis. ^{13}C NMR spectra were collected on a Bruker ARX500 spectrometer equipped with a 5 mm BBFO Z-gradient probe at ambient temperature and represent the average of 1500 scans acquired at ~0.3 scans per second.

Glucose adsorption experiments were performed using 10 cm^3 of 50 wt % aqueous D-glucose solution (pH = 4) and 0.1 g of catalytic solids for 1800 s at 373 K. Reactor contents were then quenched and centrifuged prior to decanting off the aqueous solution. Solids were dried in ambient flowing air overnight prior to removal from the reactor for X-ray absorption spectroscopy (XAS) analysis.

2.5. Computational Methods. Periodic planewave-based DFT calculations were carried out using the Vienna ab initio simulation package (VASP).[51−54] Planewaves were constructed using the projector augmented wave method (PAW) with an energy cutoff of 400 eV.[55,56] Exchange and correlation energies were computed using the revised Perdew−Burke−Ernzerhof (RPBE) form of the generalized gradient approximation.[57−59] Dispersive interactions were accounted for using the DFT-D3 method with Becke−Johnson damping (D3BJ).[60,61] The Brillouin zone was sampled using the Γ-point.[62]

Wave functions were converged to electronic energies within 10^{-6} eV; forces were determined using a fast Fourier transform (FFT) grid with a cutoff equal to twice the planewave cutoff, and structures were optimized to forces < 0.05 eV $Å^{-1}$. Transition state structures were obtained using a two-step method. First, the nudged elastic band (NEB) method[63,64] was used to approximate the minimum energy pathway using 16 images along the reaction coordinate and converging forces normal to the pathway to <0.5 eV $Å^{-1}$ while calculating forces using an FFT grid with a cutoff of 1.5 times the planewave cutoff and converging wave functions to energies within 10^{-4} eV. The approximate pathway generated by this method was used to generate input transition state geometries and reaction trajectories for the dimer method,[65] which was then used to determine transition state structures using the same electronic and structural convergence criteria described for optimizations earlier.

The Beta zeolite was modeled using a fully periodic structure obtained from the IZA-SC database of zeolite structures[66] (tetragonal, $a = b$ = 12.632 Å, c = 26.186 Å) and is structurally similar to the polymorph A structure of Beta reported elsewhere.[67] Closed Lewis acid sites were created by replacing a framework Si atom (T6 site)

DOI: 10.1021/jacs.8b08336
J. Am. Chem. Soc. 2018, 140, 14244−14266

with a Ti heteroatom, which are similar to models used in previous studies.[45] The amount of additional intraporous water (0−10 molecules) was varied to determine the effects of intraporous water content on the reaction energetics for glucose isomerization to fructose.

Desorbed glucose was modeled in vacuum and within a crystalline water structure (hexagonal ice, Ih phase). Neither of these desorbed states accurately captures the enthalpy and entropy of glucose within liquid water, but they represent extremes of enthalpic stabilization (ice) and entropic stabilization (vapor) and the upper bounds for the glucose free energy, which will be lower in the aqueous phase than in gaseous or icelike phases at reaction conditions. Inaccuracies in modeling the thermodynamics of the desorbed glucose state may introduce systematic error into the free energy values calculated in this study but will not affect the conclusions regarding the effects of intraporous water, because all reactions modeled at various water contents involve the same number of glucose adsorption events.

Frequency calculations were performed on all states (including transition states) to determine zero-point vibrational energies (ZPVEs), vibrational enthalpies (H_{vib}), and free energies (G_{vib}). The finite difference method was used with two displacements per unconstrained atom to calculate the Hessian matrix and vibrational frequencies of guest species (e.g., glucose, water) within the Beta zeolite in addition to the heteroatom and framework O bound to that heteroatom. Vibrational frequency values <60 cm^{-1} are inaccurate from fixed displacement DFT methods but are commonly observed in weakly bound species adsorbed within zeolite pores. In this work, low vibrational frequency modes (<60 cm^{-1}) were replaced with a value of 60 cm^{-1}, such that frustrated translations and rotations of weakly bound molecules contribute to entropy, while preventing exact values from being inaccurately used. These vibrational frequencies were used, together with VASP-derived electronic energies (E_0), to obtain enthalpies,

$$H = E_0 + E_d + \mathrm{ZPVE} + H_{vib} + H_{trans} + H_{rot} \quad (2)$$

and free energies,

$$G = E_0 + E_d + \mathrm{ZPVE} + G_{vib} + G_{trans} + G_{rot} \quad (3)$$

for all reactant, product, and transition state structures, where E_d is the dispersive energy estimated by DFT-D3BJ methods.[60,61] For gaseous molecules, translational and rotational enthalpies and free energies were computed from statistical mechanics.

2.6. Attenuated Total Reflectance Infrared Spectroscopy with Modulation Excitation Spectroscopy Phase-Sensitive Detection Multicurve Resolution-Alternating Least-Squares. In situ attenuated total reflectance infrared (ATR-IR) spectroscopy was used to verify the identities of the most abundant reactive intermediates (MARIs) and the structures of reactive intermediates that form on Ti-Beta surfaces during reactions with glucose. Untreated samples were ground to a fine powder (<200 mesh), and 0.03 g were suspended in 5 cm^3 of methanol (Macron Chemicals, anhydrous). A ZnSe cylindrical internal reflection element (IRE, International Crystal Laboratories) was dipped into the methanol suspension and then dried at ambient temperature. The dip-coating procedure was repeated through 10 cycles to evenly coat the IRE with a thin layer of catalyst material. The coated IRE was then loaded into a customized ATR flow cell (Axiom TNL-120) equipped with two liquid inlets and one outlet with a cell volume of 40 μL. The ATR cell was mounted within the sample compartment of a FTIR spectrometer (Bruker, Vertex 70 RapidScan) equipped with a liquid N_2 cooled HgCdTe detector. Liquid streams of pure water and 50 wt % glucose in water were introduced at controlled flow rates using two high-pressure piston pumps (SSI series 1), which were controlled using LabVIEW. The cell was heated by a resistive heating cartridge placed within the wall of the cell. A K-type thermocouple (Omega) placed adjacent to the IRE at the center of the z-axis measured the temperature, which was controlled by an electronic temperature controller (Watlow, EZ-Zone). Background scans were obtained under steady-state conditions flowing 1 cm^3 min^{-1} of pure deionized water at 373 K after loading the ATR cell. Spectra obtained during transient cutoff experiments were collected at a resolution of 4 cm^{-1} and averaged over 4 scans. Spectra obtained during modulation experiments were collected at a resolution of 1 cm^{-1} and averaged over 64 scans. All spectra acquisitions were performed using Bruker Corporation's OPUS Spectroscopy software 7.0.129.

Modulation excitation spectroscopy (MES) is a powerful technique in which a periodic stimulation is applied to the system while acquiring spectra as a function of time. The time-domain response is then converted to a phase-domain response, and only spectral features that change in synchrony with the applied stimulation are extracted using a phase-sensitive detection (PSD) method described by the following equation:

$$A_k(\varphi_k^{PSD}) = \frac{2}{T}\int_0^T A(t)\sin(k\omega t + \varphi_k^{PSD})\,dt \quad (4)$$

Here, $A(t)$ and $A_k(\varphi_k^{PSD})$ are time-domain and phase-domain responses of the measured species, respectively, T is the period of the applied stimulus in seconds, ω is the demodulation index, and φ_k^{PSD} is the user-defined phase demodulation angle. The application of the MES-PSD technique to FTIR spectra of intermediates on catalytic surfaces reveals spectra that only contain contributions from intermediates that change as a result of the applied stimulus (e.g., changing reactant concentrations) under relevant conditions and, in doing so, simultaneously reduces contributions from random sources of spectral noise.[68] Here, concentrations of glucose and water were modulated sinusoidally by controlling the flow rate of liquid through the two piston pumps and set specifically such that the set points of the pumps were changed in a stepwise manner every 0.5 s to approximate a sine wave with the desired frequency. Recorded time-domain spectra were resampled to a single period, and subsequently the spectra of the active species were extracted by PSD using eq 4. The resultant phase-domain spectra reflect contributions from multiple species that oscillate at the same frequency as the applied stimulus, and these chemically distinct species may be separated using principle component analyses that recognize the different phase delays of kinetically distinct groups of species. Multicurve resolution-alternating least-squares (MCR-ALS) analysis was performed to extract the spectra and concentration profiles (or surface coverages) of independent species from the phase-domain spectra (additional details in Section S.4.1, Supporting Information) using a recently published MATLAB code.[69]

2.7. X-ray Absorption Spectroscopy Measurements. Ti K-edge (4.966 keV) XAS measurements were performed on the bending magnet beamline of the Materials Research Collaborative Access Team (MRCAT) at the Advanced Photon Source at Argonne National Laboratory. Measurements were taken in step-scan transmission mode with a Ti foil reference spectrum collected simultaneously using a third ion chamber in series for energy calibration. Samples were pressed into a stainless-steel sample holder containing six wells and placed in a quartz reactor tube with Kapton windows. The reactor was purged with He prior to collecting measurements on the hydrated samples to minimize photon absorption by the gas phase. Spectra were collected under ambient conditions prior to heating the samples in flowing He to 523 K for 30 min. Samples were then cooled to room temperature prior to collection of dehydrated spectra.

XAS data were analyzed using WinXAS 3.2 software[70] for spectra normalization and background subtraction. Coordination parameters were obtained via simultaneous R-space least-squares fits of the magnitude and imaginary component of the k^2-weighted EXAFS Fourier transform (Δk = 2.90−10.0 $Å^{-1}$). Experimental phase-shift and back-scattering amplitude fitting functions for Ti−O scattering paths were obtained from the TiO_2 anatase phase (6 Ti−O bonds at 1.96 Å).

3. RESULTS AND DISCUSSION

3.1. Bulk Structural and Lewis Acid Site Characterization of Ti-Beta Zeolites. Ti-Beta zeolites were crystallized via direct hydrothermal synthesis in fluoride media (Ti-Beta-F)

DOI: 10.1021/jacs.8b08336
J. Am. Chem. Soc. 2018, 140, 14244−14266

Table 1. Active Site and Structural Characterization Data for Ti-Beta Samples

sample	V_{ads} (N_2, 77 K)[a] (cm^3 g^{-1})	edge energy[b] (eV)	Lewis acidic Ti density[c] (10^{-5} mol Ti_{LA} g^{-1}, CD_3CN)	Lewis acidic Ti density[d] (Ti_{LA} unit $cell^{-1}$, CD_3CN)	fraction of Lewis acidic Ti[e]	Lewis acidic Ti density[f,g] (10^{-5} mol Ti_{LA} g^{-1}, pyridine)
Ti-Beta-F-133	0.21	5.3	4.17	0.16	0.34	n.m.
Ti-Beta-F-135	0.19	4.5	3.93	0.15	0.32	6.35
Ti-Beta-F-142	0.20	4.3	6.70	0.26	0.58	8.40
Ti-Beta-F-143	0.21	4.2	4.63	0.18	0.40	6.51
Ti-Beta-F-155	0.20	5.3	6.64	0.26	0.62	4.64
Ti-Beta-F-170	0.20	5.3	2.36	0.09	0.24	4.87
Ti-Beta-F-180	0.22	4.4	2.99	0.12	0.33	n.m.
Ti-Beta-F-282	0.20	5.1	0.89	0.03	0.15	n.m.
Ti-Beta-OH-34	0.22	4.5	18.77	0.72	0.40	16.85
Ti-Beta-OH-38	0.19	4.7	14.80	0.57	0.35	n.m.
Ti-Beta-OH-46	0.23	4.4	35.20	1.36	1.00	36.29
Ti-Beta-OH-71	0.21	4.7	13.08	0.50	0.57	11.79
Ti-Beta-OH-297	0.18	4.5	26.88	1.03	0.32	32.70

[a]N_2 volumes at the end of micropore filling transition (77 K). [b]Determined from Tauc plots after dehydration (523 K). [c]Lewis acidic Ti densities measured from CD_3CN titration IR experiments. [d]Lewis acidic Ti densities measured from CD_3CN titration IR experiments normalized per unit cell. [e]Fraction of total Ti concentration present as Lewis acidic Ti sites measured from CD_3CN titration IR experiments. [f]Lewis acidic Ti densities measured from pyridine titration IR experiments. [g]n.m.: not measured.

and via post-synthetic grafting of $TiCl_4$ into framework defect vacancies of dealuminated Beta supports (Ti-Beta-OH; residual Si/Al > 1500). Relevant structural characterization data on these samples are summarized in Table 1. X-ray diffraction patterns and micropore volumes measured from N_2 adsorption isotherms (77 K) of all samples were consistent with the Beta topology (Figures S.1 and S.2, Supporting Information). The higher signal-to-noise XRD patterns measured for Ti-Beta-F samples reflect crystallites that are larger (~3−12 μm) than Ti-Beta-OH samples (~0.6−1.2 μm), consistent with average crystallite sizes determined from SEM images (Figures S.3 and S.4, Supporting Information) and as expected from prior reports.[31,71] Crystallite sizes of all Ti-Beta-OH samples prepared post-synthetically resemble those of their dealuminated and parent Al-Beta samples, which vary with Al content and crystallization time (Figure S.5, Supporting Information).[71,72] UV−visible spectra on Ti-Beta-F and Ti-Beta-OH samples (Figures S.6 and S.7, Supporting Information) collected after dehydration treatments (523 K) were used to estimate edge energies (4.2−5.3 eV, Table 1) from Tauc plots (Figures S.8 and S.9 and Table S.1, Supporting Information) that are characteristic of isolated Ti^{4+} centers within zeolite frameworks (≥4.1 eV).[73] These bulk characterization data indicate that this suite of Ti-Beta samples contains framework Ti centers of widely varying content (Si/Ti = 34−297; 0.09−1.36 Ti per unit cell).

The fraction of Ti^{4+} sites that behave as Lewis acid centers was quantified from IR spectra collected after titration by CD_3CN at 303 K. Figure 1 shows IR spectra for ν(C≡N) stretching vibrations on Ti-Beta-F-155 with increasing CD_3CN coverage (spectra of Ti-Beta-OH-46 in Figure S.10, Supporting Information). At low CD_3CN coverages (CD_3CN/Ti = 0.2−0.6), a peak centered at 2308 cm^{-1} for CD_3CN adsorbed at Lewis acidic Ti sites appears first, followed by peaks for CD_3CN bound to silanol groups (2275 cm^{-1}) and for gas-phase or physisorbed CD_3CN (2265 cm^{-1}),[74] indicating that CD_3CN preferentially adsorbs onto framework Lewis acidic Ti sites over silanol defects. The 2308 cm^{-1} peak increases in area with subsequent CD_3CN exposure until saturation coverages are reached. Integrated areas for the 2308 cm^{-1} peak were quantified from deconvoluting IR spectra into their 2308, 2275, and 2265 cm^{-1} components (Figure S.11, Supporting Information), using a previously reported procedure to isolate component peaks for CD_3CN bound to hydrolyzed-open

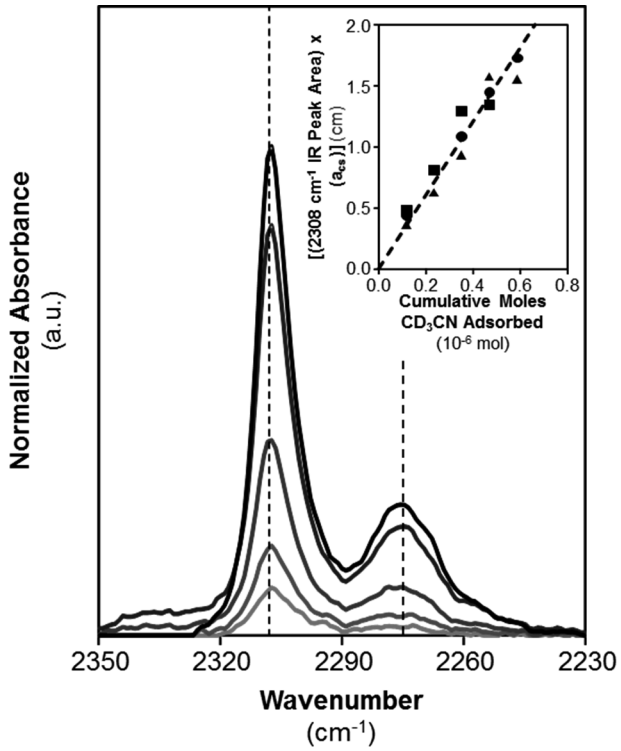

Figure 1. CD_3CN IR spectra of the ν(C≡N) stretching region with increasing coverage of CD_3CN on Ti-Beta-F-155 (0.013, 0.026, 0.065, 0.170, and 0.235 CD_3CN/Ti, light to dark). Dashed vertical lines correspond to 2308 and 2275 cm^{-1} for ν(C≡N) stretching vibrations of CD_3CN bound to Lewis acidic Ti sites and silanol groups, respectively. The inset shows the integrated area of the 2308 cm^{-1} peak multiplied by the cross-sectional area of the IR wafer, plotted against the moles of CD_3CN adsorbed at Lewis acidic Ti sites for Ti-Beta-F-155 (●), Ti-Beta-F-135 (■), and Ti-Beta-OH-38 (▲). The dashed line in the inset is the best fit line through all data, with the slope representing the integrated molar extinction coefficient for CD_3CN adsorbed onto Lewis acidic Ti sites.

DOI: 10.1021/jacs.8b08336
J. Am. Chem. Soc. 2018, 140, 14244−14266

Table 2. Semiquantitative Measurements of the Hydrophobic Properties of Microporous Voids in Ti-Beta-F and Ti-Beta-OH Materials

sample	silanol density[a] (10^{-4} mol SiOH g^{-1})	silanol density[b] (mol SiOH mol Ti_{LA}^{-1})	V_{ads} (H_2O, 293 K)[c] (10^{-3} cm^3 g^{-1}, P/P_0 = 0.2)	normalized V_{ads} (H_2O, 293 K)[d] (cm^3 g^{-1})	V_{ads} (H_2O)/V_{ads} (N_2)[e]	V_{ads} (CH_3OH)[f] (cm^3 g^{-1})
Ti-Beta-F-133	1.21	2.9	2.31	0.04	0.011	0.062
Ti-Beta-F-135	0.86	2.2	2.02	0.03	0.011	0.072
Ti-Beta-F-142	1.54	2.3	2.53	0.01	0.013	0.083
Ti-Beta-F-143	1.32	2.8	3.52	0.10	0.017	0.080
Ti-Beta-F-155	1.93	2.9	4.48	0.12	0.022	0.051
Ti-Beta-F-170	0.65	2.8	3.10	0.12	0.015	0.082
Ti-Beta-F-180	1.66	5.5	3.88	0.16	0.018	0.062
Ti-Beta-F-282	0.29	3.2	1.33	0.06	0.007	0.035
Ti-Beta-OH-34	6.72	3.6	46.39	2.20	0.211	1.04
Ti-Beta-OH-38	14.79	10.0	93.57	4.90	0.492	0.98
Ti-Beta-OH-46	7.02	2.0	37.93	1.40	0.165	0.33
Ti-Beta-OH-71	7.97	6.1	41.77	2.06	0.199	1.09
Ti-Beta-OH-297	6.28	2.3	53.03	2.41	0.295	1.19
Si-Beta-F			2.20	2.20		

[a]Silanol densities measured from CD_3CN titration IR experiments. [b]Silanol densities normalized by Lewis acidic Ti densities measured from CD_3CN titration IR experiments. [c]Water volumes at P/P_0 = 0.2 (293 K). [d]Water volumes at P/P_0 = 0.2 (293 K) after normalization by two times the number of Lewis acidic Ti sites determined from CD_3CN titration IR experiments. [e]Fraction of total micropore volume filled by water at P/P_0 = 0.2 (293 K). [f]CH_3OH volumes taken at the end of the first adsorption regime (293 K), indicative of adsorbate−adsorbent interactions. This corresponds to low P/P_0 values (0.02−0.04) for type V isotherms on Ti-Beta-F samples and the highest measured P/P_0 values (0.6−0.7) on Ti-Beta-OH samples.

($Sn(OH)(OSi)_3$, 2316 cm^{-1}) and closed ($Sn(OSi)_4$, 2308 cm^{-1}) Sn sites within Sn-zeolites.[32]

The inset of Figure 1 shows the integrated area for the 2308 cm^{-1} peak as a function of the number of CD_3CN molecules bound to Lewis acidic Ti sites (Ti_{LA}), determined in coverage ranges (CD_3CN/Ti = 0.2−0.6) that correspond to equimolar titrant-to-site binding stoichiometry. Integrated 2308 cm^{-1} peak areas increase linearly with the amount of CD_3CN adsorbed onto Lewis acidic Ti sites, and in an equivalent proportion for three Ti-Beta samples of different Ti contents and synthetic origins (Ti-Beta-F-155, Ti-Beta-F-135, and Ti-Beta-OH-38). This proportion reflects the integrated molar extinction coefficient for this IR peak (E(2308 cm^{-1}) = 3.01 ± 0.60 cm μmol^{-1}) via eq 1. This E(2308 cm^{-1}) value was then used to quantify Lewis acidic Ti sites on each Ti-Beta sample after saturation with CD_3CN and deconvolution of IR spectra (Figure S.12, Supporting Information). Site quantification values are reported in Table 1 as the fraction of Lewis acidic Ti sites titrated by CD_3CN (per total Ti). Dichloromethane-assisted grafting of $TiCl_4$ within framework vacancies of dealuminated Beta zeolites formed Ti-Beta-OH samples that generally contained higher fractions of Lewis acidic Ti sites (0.40−1.00, Table 1) than fluoride-mediated, hydrothermally synthesized Ti-Beta-F samples (0.24−0.62, Table 1). The numbers of Lewis acid sites quantified by CD_3CN on these Ti-Beta samples are consistent with the numbers quantified by pyridine titration (0.38−1.03 Lewis acid sites per Ti, E(1605 cm^{-1}) = 1.16 ± 0.23 cm μmol^{-1}; details in Section S.1.2, Supporting Information). The fraction of Lewis acidic Ti species are below unity for most samples, necessitating such site quantification techniques to normalize catalytic rate measurements because residual Ti species reflect small TiO_2 domains that do not contribute to measured glucose−fructose isomerization rates.[42]

Exposure to higher CD_3CN pressures gives rise to IR peaks centered at 2275 cm^{-1} that reflect CD_3CN bound to silanol defects (Figure S.10, Supporting Information). Using an integrated molar extinction coefficient (E(2275 cm^{-1}) = 0.74 ± 0.16 cm μmol^{-1}) determined previously from CD_3CN IR spectra of a dealuminated Beta sample,[32] the total number of silanol defects was estimated for each Ti-Beta sample and is listed in Table 2. Silanol groups are present in significantly higher densities (~4−100×) on Ti-Beta-OH than on Ti-Beta-F samples, as expected for Ti-Beta-OH samples that contain silanol groups formed during the hydrothermal synthesis of the parent Al-Beta zeolite in hydroxide media and silanol nest defects that remain after partial grafting with Ti precursors. CD_3CN does not discriminate between silanol groups located within microporous voids from those located at extracrystalline surfaces, which may be present in higher concentrations on smaller Ti-Beta-OH crystallites than on larger Ti-Beta-F crystallites (~0.9 vs 7.5 μm, Figures S.3−S.5, Supporting Information). These total silanol concentrations, however, do not correlate with external crystallite surface areas among the Ti-Beta-F and Ti-Beta-OH samples studied here (details in Section S.1.3, Supporting Information), implying that higher defect densities are present within the microporous channels of Ti-Beta-OH.

From these characterization data, we conclude that the synthesized Ti-Beta-F and Ti-Beta-OH samples are crystalline Beta zeolites that contain varying quantities of Ti atoms located within framework positions and that behave as Lewis acid centers. Furthermore, CD_3CN titration experiments indicate that Ti-Beta-OH samples contain significantly higher bulk silanol densities than Ti-Beta-F samples. We next use a suite of adsorption and spectroscopic probes that are sensitive to the location of silanol groups within microporous voids to provide evidence that the density of silanol defects is higher within the microporous voids of Ti-Beta-OH than in Ti-Beta-F.

3.2. Characterization of Hydrophobic Properties of Ti-Beta Zeolites. In this section, we compare the polarity of microporous voids in Ti-Beta-F and Ti-Beta-OH samples by combining semiquantitative assessments of vapor-phase water

DOI: 10.1021/jacs.8b08336
J. Am. Chem. Soc. 2018, 140, 14244−14266

and methanol adsorption isotherms with structural assessments of adsorbed water phases from IR spectra collected in the presence of water vapor. Taken together, these data reveal differences in the intraporous density of polar silanol groups within microporous voids of Ti-Beta-F and Ti-Beta-OH and in the structures of water stabilized within these voids.

3.2.1. Semiquantitative Assessments of Hydrophobicity Using Vapor-Phase Adsorption Isotherms. Water adsorption isotherms provide an assessment of the hydrophobic properties of zeolitic surfaces, as bulk water uptakes increase with the density of polar defect sites (e.g., framework heteroatoms, hydroxyl groups) located in otherwise nonpolar siloxane frameworks.[32,47] Vapor-phase water adsorption isotherms of Ti-Beta-F samples (Figure S.16, Supporting Information) show water uptakes similar to Si-Beta-F (within 2.5×, 293 K, P/P_0 = 0−0.6), suggesting that surfaces with low defect densities are also present within Ti-Beta-F micropores.[31] Table 2 summarizes the total water uptake per gram at P/P_0 = 0.2, a parameter that allows for semiquantitative comparison of hydrophobicity among samples and which corresponds to the reduced pressure required for micropore filling of cyclohexane within hydrophobic MOR zeolites.[49] Table 2 also summarizes the residual water uptakes after subtraction of two water molecules adsorbed per Lewis acid site, a stoichiometry that has been observed experimentally from gravimetric and microcalorimetric studies on Ti-Beta zeolites for water adsorption on isolated framework Ti sites.[30] Water uptakes (per g) at a given reduced pressure are systematically higher on Ti-Beta-F than on Si-Beta-F samples but are similar (within 1.5×) after accounting for two water molecules adsorbed onto Lewis acidic Ti site. These low water uptakes ($V_{ads}(H_2O)/V_{ads}(N_2)$ = 0.001−0.011, Table 2) reflect the hydrophobic nature of intraporous void environments, consistent with water intrusion studies in defect-free siliceous Beta zeolites that require significantly higher water pressures (57 MPa) for pore filling.[75] Hydrophobic channels in Beta zeolites (∼0.7 nm diameter) mitigate the formation of bulk water structures under ambient conditions because polar surface groups capable of hydrogen bonding are absent,[31] consistent with findings from experimental studies of defect-free carbon nanotubes (<1 nm diameter)[9] and from computational studies identifying the presence of only vapor-phase water between hydrophobic pure-silica surfaces positioned 0.7 nm apart.[10]

Among the Ti-Beta-OH samples studied here, vapor-phase water adsorption isotherms (Figure S.17, Supporting Information) showed water uptakes that were 10−40× higher than on Ti-Beta-F samples (293 K, P/P_0 = 0−0.6) after accounting for two water molecules adsorbed onto each Lewis acid site (Table 2). These order of magnitude higher water uptakes indicate the presence of additional water adsorption sites on Ti-Beta-OH samples, which have ∼4−100× higher silanol defect densities than Ti-Beta-F as measured by CD_3CN IR (Table 2). Indeed, a linear correlation between total silanol concentration (per g) and water uptake (per g, P/P_0 = 0.2) is observed among all Ti-Beta-F and Ti-Beta-OH samples studied (Figure S.18, Supporting Information), which has previously been noted among Sn-Beta samples[32] and among H-form FAU, MFI, and Beta samples.[27] These findings are qualitatively consistent with computational studies indicating that extended water structures (up to 27 molecules) can be stabilized when two adjacent silanol defects are present between hydrophobic SiO_2 plates positioned 0.7 nm apart.[10] These water adsorption uptakes and silanol density measurements reflect bulk properties of zeolite samples, however, and do not provide direct information about the density of silanol defects within microporous environments.

In contrast to water, methanol fills microporous voids in both low-defect and high-defect samples, but with distinct adsorption behavior. Methanol adsorption isotherms (293 K) on low-defect Ti-Beta-F samples show type V isotherm behavior (Figure S.19, Supporting Information), reflecting micropore condensation driven by adsorbate−adsorbate interactions that are stronger than adsorbate−adsorbent interactions of methanol with nonpolar framework siloxane linkages,[31,41,47,76] as observed previously for ethanol within hydrophobic Ti-Beta-F[31] and Si-MFI.[77] In contrast, methanol adsorption isotherms on Ti-Beta-OH materials show type I isotherm behavior (Figure S.20, Supporting Information), reflecting micropore condensation driven by strong adsorbate−adsorbent interactions through methanol hydrogen-bonding interactions with specific binding sites located on micropore walls. These adsorption sites are not Lewis acidic Ti sites, evident from the direct comparison of Ti-Beta-F-155 and Ti-Beta-OH-71, which contain similar Lewis acid site densities (0.26 and 0.50 per unit cell, respectively, Table 1) but show significant differences in adsorption behavior. The type I isotherms on Ti-Beta-OH therefore reflect the presence of silanol defects located within microporous channels that hydrogen bond with methanol, while the type V isotherms on Ti-Beta-F reflect essentially undetectable amounts of silanol groups or other hydrogen-bonding moieties located within the microporous channels of Ti-Beta-F.[23]

3.2.2. Spectroscopic Characterization of Coadsorbed Water Structures Using Transmission IR. Transmission IR spectroscopy was used to probe differences in the vibrational signatures and extended structures of adsorbed water on Ti-Beta-F-155 and Ti-Beta-OH-46, which are representative Ti-Beta-F and Ti-Beta-OH samples from bulk characterization data, Lewis acid site densities, and glucose−fructose isomerization-rate measurements (see Tables 1 and 2 and Section 3.3). Parts A and B of Figure 2 show IR spectra collected on Ti-Beta-F-155 and Ti-Beta-OH-46 after removing background contributions for water vapor present in the cell and subtracting the spectrum of dehydrated zeolite samples (full spectra in Figure S.21, Supporting Information). Upon equilibration in flowing water, two prominent features appear as positive broad peaks in the 1500−1750 cm^{-1} range and the 2600−3700 cm^{-1} range, while a third negative peak appears centered around 3735−3745 cm^{-1}.

Figure 2A shows the IR peak centered between 1615−1630 cm^{-1}, which reflects the δ(H−O−H) scissoring mode of adsorbed water.[78] This peak does not significantly change shape or center with increasing water uptake. The integrated area of this peak is proportional to the total water uptake (at equivalent reduced pressures) estimated from vapor-phase adsorption experiments (298 K, Figure S.22, Supporting Information), as shown in the inset of Figure 2A. The linear relation in the inset of Figure 2A establishes a direct connection between the total water uptake and each IR spectrum as quantified through the integrated area of the 1615−1630 cm^{-1} peak.

Figure 2B shows a negative peak (3735−3745 cm^{-1}) on both samples reflecting a convolution of two peaks centered at 3745 and 3735 cm^{-1} for OH stretching modes of external and internal silanol groups, respectively.[79] These features appear as negative peaks because hydrogen-bonding interactions be-

DOI: 10.1021/jacs.8b08336
J. Am. Chem. Soc. 2018, 140, 14244−14266

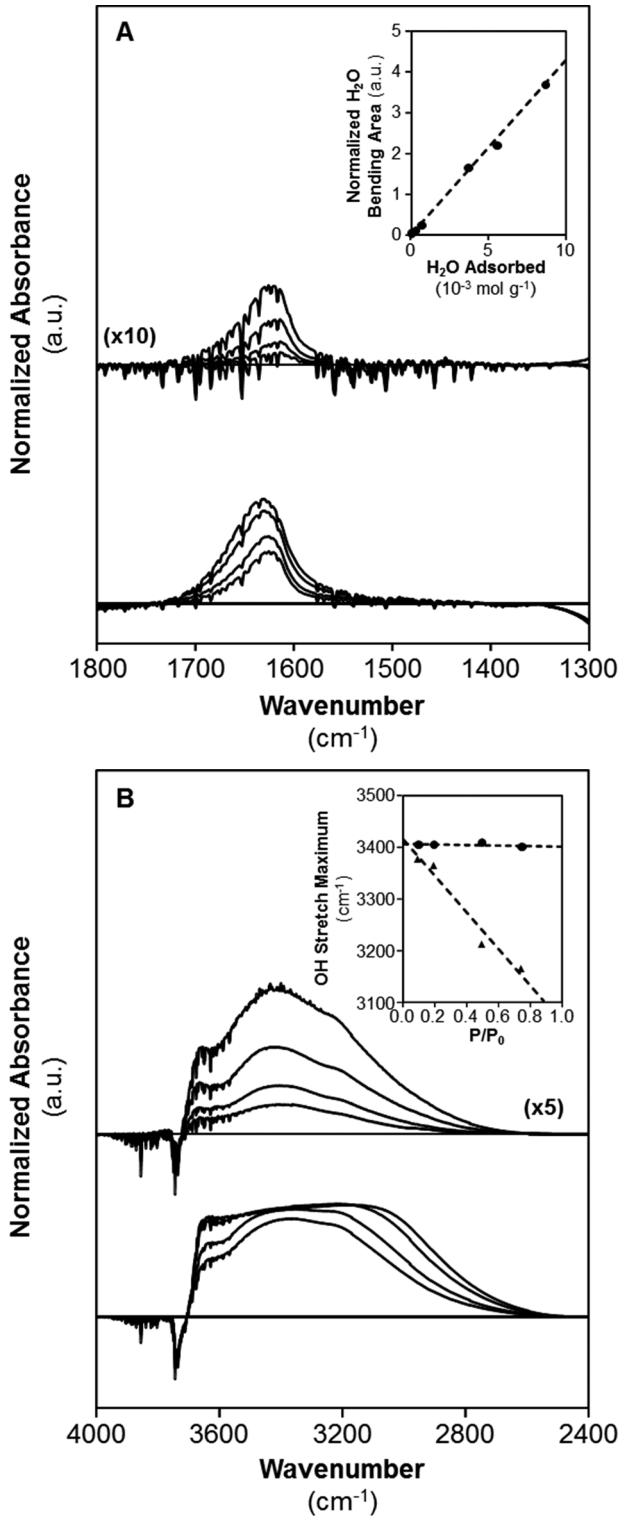

Figure 2. Baseline-corrected difference IR spectra of adsorbed water on Ti-Beta-F-155 (top, magnified for clarity) and Ti-Beta-OH-46 (bottom) at 298 K for (a) δ(HOH) scissoring modes in the water bending region and (b) the ν(O−H) water-stretching region. Difference spectra reflect the subtraction of the spectrum measured on the sample under vacuum prior to water flow and corrected for background water adsorption onto the IR cell. Spectra for each sample displayed from bottom to top correspond to P/P_0 = 0.1, 0.2, 0.5, and 0.75. The insets display the change in (a) the water bending peak area and (b) the water-stretching peak maximum with increasing water concentration for Ti-Beta-F-155 (●) and Ti-Beta-OH-46 (▲).

tween adsorbed water and hydroxyl groups perturb silanol O−H stretches, giving rise to the broad positive peak centered around 3400 cm^{-1}. Difference spectra on Ti-Beta-OH-46 do not show further changes to the negative peak areas at 3745 and 3735 cm^{-1} at relative water pressures of $P/P_0 \geq 0.2$, indicating that the hydroxyl groups are fully perturbed by hydrogen-bonded water by P/P_0 = 0.1 (Figure S.23, Supporting Information). Therefore, subsequent adsorption of water above this relative pressure occurs via hydrogen bonding with other water molecules already present within the channels, rather than through additional adsorption at silanol defects. In contrast, the silanol groups on Ti-Beta-F-155 continue to be perturbed gradually across a wider range of water pressures (P/P_0 = 0.1−0.75, Figure S.23, Supporting Information), indicating that water adsorption continues to occur at silanol defects. These observations are consistent with lower water uptakes from vapor-phase adsorption isotherm experiments, suggesting that water does not fill the micropores of Ti-Beta-F-155 under these conditions. Hence, water adsorbs within Ti-Beta-F at low intraporous densities (0.01−0.16 mol of H_2O g^{-1}, Table 2) because it predominantly adsorbs at framework Ti sites, but within Ti-Beta-OH with higher intraporous water densities (1.4−4.9 mol of H_2O g^{-1}, Table 2) because it adsorbs at both framework Ti atoms and silanol defects.

The OH stretching vibrations from adsorbed water molecules are convoluted with the perturbed silanol peak in the 2600−3700 cm^{-1} range, yet differences regarding the structure of adsorbed water in Ti-Beta-OH-46 and Ti-Beta-F-155 are readily apparent. With increasing water partial pressure (P/P_0 = 0.1−0.75), the peak maximum in the OH stretching region monotonically shifts from 3375 to 3190 cm^{-1} on Ti-Beta-OH-46 (Figure 2B, inset). Shifts in OH stretching frequency to lower wavenumbers reflect greater extents of hydrogen bonding between water molecules,[14,80] suggesting that adsorbed water molecules within Ti-Beta-OH-46 become arranged in extended hydrogen-bonding networks that grow with increasing water partial pressure. In addition, this broad peak for adsorbed water can be deconvoluted into two major components centered in either the ∼3000−3100 cm^{-1} range or the 3630−3665 cm^{-1} range. The latter peak (3630−3665 cm^{-1}) has been assigned to loosely bound water in one-dimensional chains that are similar in their extent of hydrogen bonding to vapor-phase water located within nonpolar carbon nanotubes (<0.8 nm in diameter)[14] similar in size to Beta micropores. Thus, the continued presence of this peak at higher water partial pressures ($P/P_0 \geq 0.2$) indicates that some water molecules are occluded within microporous voids and can plausibly be considered vapor-like. The peak ranging from ∼3000−3100 cm^{-1} is shifted to lower wavenumbers than that of OH stretches in bulk ice (3220−3250 cm^{-1}),[81] reflecting contributions of water molecules in extended hydrogen-bonding networks. As the water partial pressure increases, this peak becomes more prominent and eventually reflects the hydrogen-bonded structure of the majority of occluded water molecules within the channels of Ti-Beta-OH-46.

The structure of water adsorbed within Ti-Beta-F-155 sharply contrasts that of Ti-Beta-OH-46. First, the water OH stretching peak center remains constant at ∼3400 cm^{-1} in Ti-Beta-F-155 with increasing water partial pressure (Figure 2B, inset), reflecting weaker contributions from strongly hydrogen-bound water stretches in the ∼3000−3100 cm^{-1} range. This provides evidence that adsorbed water molecules in Ti-Beta-F-

DOI: 10.1021/jacs.8b08336
J. Am. Chem. Soc. 2018, 140, 14244−14266

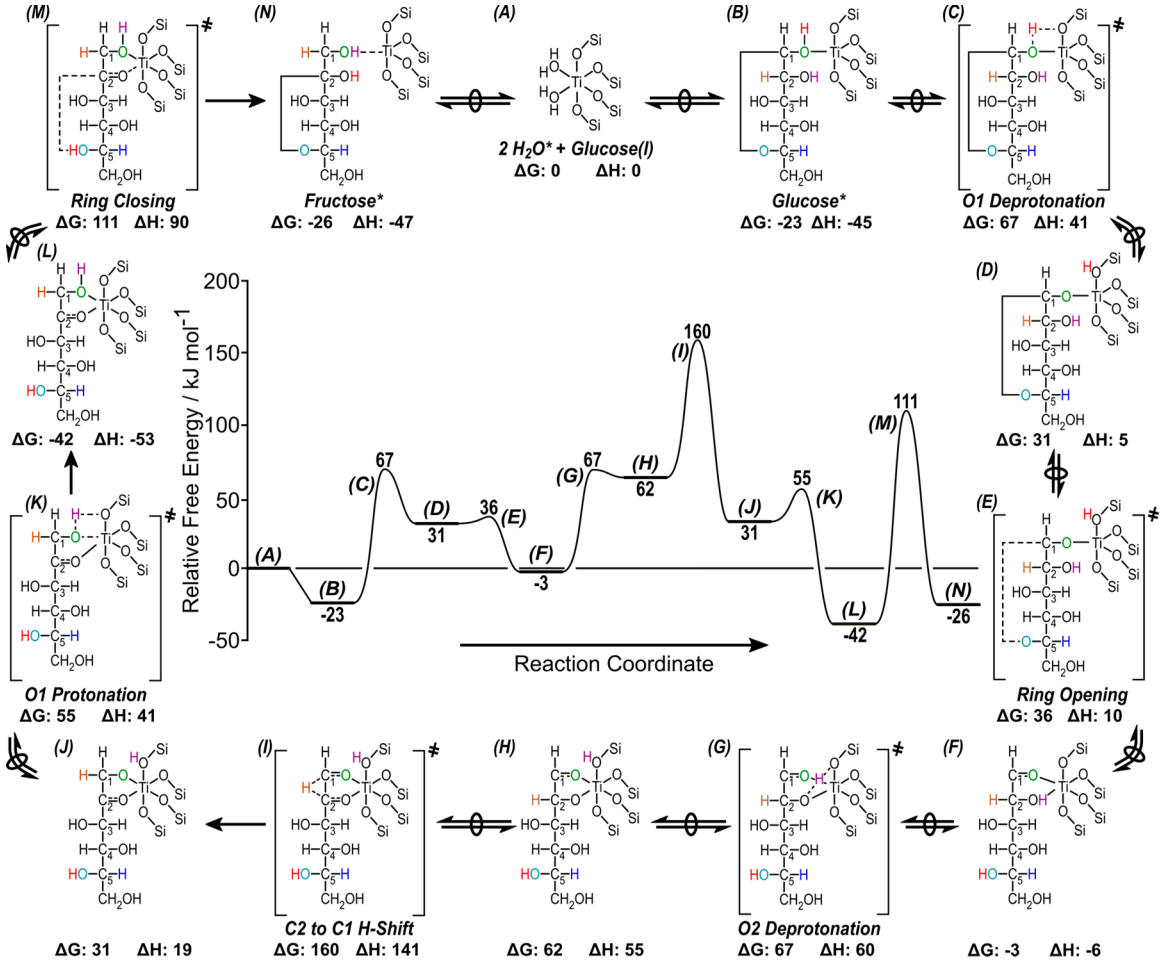

Figure 3. Free energy (373 K, 1 bar) reaction coordinate diagram for the formation of fructose from glucose on closed Ti Lewis acid sites. Reaction arrows with overlaid circles indicate quasi-equilibrated events or the formation of transition states from relevant precursors. Relative enthalpies are given near inset images.

155 do not significantly increase their extent of hydrogen bonding with increasing water pressure, nor do they form the extended water structures observed in Ti-Beta-OH-46. Indeed, further adsorption of water perturbs additional silanol groups throughout this partial pressure range, evident in increasingly negative peak area for the peak centered at 3735−3745 cm^{-1} and in increasingly positive peak area for the peak centered at ∼3400 cm^{-1} (Figure S.23, Supporting Information). A small shoulder present at ∼3100 cm^{-1} in the difference spectra of Ti-Beta-F-155 (Figure 2B) increases in area with increasing water partial pressure, however, indicating that some water molecules adsorb via hydrogen bonding in locations with proximal water molecules, but to a much lesser extent than in Ti-Beta-OH-46. The significantly lower water uptakes (Figure S.22, Supporting Information) suggest that the lower silanol defect density in Ti-Beta-F-155 (1.9×10^{-4} mol SiOH g^{-1}, Table 2) is insufficient to nucleate the formation of extended hydrogen-bonded water structures within the pores, in contrast to the behavior of water adsorption on Ti-Beta-OH-46 (7.0×10^{-4} mol SiOH g^{-1}, Table 2).

From these characterization data in Sections 3.1 and 3.2, we conclude that the series of samples investigated here contain Ti centers isolated within Beta molecular sieve frameworks over a wide range of Ti content (Si/Ti = 38−297) and residual silanol defect densities ($SiOH/Ti_{LA}$ = 2.0−10, Table 2). Water adsorbs preferentially within zeolite Beta micropores at framework Ti atoms, and at surface silanol groups via hydrogen bonding. Methanol adsorption isotherms indicate that Ti-Beta-OH has a significantly higher intraporous silanol defect density than Ti-Beta-F, leading to increased water uptakes and the stabilization of extended hydrogen-bonding water structures within their microporous voids. To determine the kinetic consequences of these intraporous silanol defects and the extended solvent structures they stabilize, we next interrogate Ti-Beta-F and Ti-Beta-OH samples using aqueous-phase glucose isomerization as a catalytic probe reaction.

3.3. Aqueous-Phase Glucose Isomerization Mechanisms and Kinetic Measurements. In this section, we combine insights from experiment and theory to elucidate the underlying phenomena that lead to differences in measured reaction kinetics for Lewis acid-catalyzed glucose isomerization in low-defect and high-defect Ti-Beta zeolites. We use a mechanistic model to identify key differences in glucose isomerization reaction coordinates in terms of free energies of reactive intermediates and transition states that are influenced by intraporous silanol defects and the extended solvent structures they stabilize.

3.3.1. Mechanistic Details of Lewis Acid-Catalyzed Glucose Isomerization. Figure 3 shows the free energy reaction coordinate diagram for glucose−fructose isomerization calculated over a framework-coordinated, closed Lewis acidic Ti site at the T6 position in Beta through a mechanism

DOI: 10.1021/jacs.8b08336
J. Am. Chem. Soc. 2018, 140, 14244−14266

similar to those reported in previous experimental and theoretical studies.[45,82] Lewis acid-catalyzed glucose isomerization to fructose occurs through quasi-equilibrated adsorption of glucose onto Lewis acid sites through the hemiacetal oxygen (O5), quasi-equilibrated deprotonation of O1 (states B−D, Figure 3), followed by protonation of the ring ether oxygen (O5) to facilitate ring opening to form the acyclic, or open-chain, glucose intermediate bound through the carbonyl moiety (states D−F, Figure 3).[82] Subsequent deprotonation of the C2 alcohol to a proximal proton acceptor, such as a nearby framework oxygen, generates a glucose intermediate that can bind to the Lewis acid site in a bidentate fashion (states F−H, Figure 3). Glucose deprotonation and ring-opening steps have kinetically irrelevant barriers, consistent with previous findings.[82] The open-chain glucose intermediate then undergoes a kinetically relevant 1,2-hydride shift to form a bound acyclic fructose intermediate, an elementary step that has the largest computed free energy barrier in the reaction coordinate (states H−J, Figure 3).[82,83] Protonation of the fructose C1 alcohol, ring closure, and desorption of fructose from the Lewis acid site closes the catalytic cycle via kinetically irrelevant steps. The overall free energy barrier to form fructose from desorbed glucose is 160 kJ mol^{-1} (373 K) when using ring-closed glucose in crystalline ice as the reference state for desorbed glucose. The overall free energy barrier from the adsorbed glucose state is 183 kJ mol^{-1} (373 K). This Lewis acid-catalyzed intramolecular 1,2-hydride shift mechanism is dominant over the base-catalyzed enolate mechanism under the conditions studied here, as reported in previously published isotopic tracer studies (see Figure S.24, Supporting Information, for ^{13}C NMR spectra of monosaccharide products).[84]

Glucose isomerization over Ti-Beta zeolites also forms sorbose, a second monosaccharide product formed through a parallel pathway and reaction mechanism analogous to that of fructose formation (free energy reaction coordinate diagram in Figure S.25, Supporting Information).[85] Isomerization to sorbose involves quasi-equilibrated glucose adsorption, deprotonation of the O1 alcohol moiety, and ring-opening to form a bidentate-bound glucose-derived intermediate through O1 and O5 (states B−D, Figure S.25, Supporting Information). This is followed by a kinetically relevant 1,5-hydride shift step (states D−F, Figure S.25, Supporting Information), as previously observed by isotopic tracer studies on ^{2}H- and ^{13}C-labeled glucose[85] and confirmed in this work (see Figure S.24, Supporting Information, for ^{13}C NMR of monosaccharide products). The 1,5-hydride shift transition state that forms sorbose is analogous to the 1,2-hydride shift that forms fructose, in that both involve six-membered ring structures and a C−H bond scissoring mode along the reaction coordinate. The catalytic cycle for sorbose formation is closed via protonation, ring closure, and desorption (states F−H, H−J, and J−A, respectively, Figure S.25, Supporting Information). The overall free energy barrier relative to the desorbed glucose state is 154 kJ mol^{-1} (373 K) and suggests that the 1,5-hydride shift is the sole kinetically relevant step, as expected;[85] all other barriers are at least 25 kJ mol^{-1} lower. Free energy barriers for fructose and sorbose formation are similar within the error of DFT, as expected for two parallel reactions with reported initial rates within 1 order of magnitude.[42,85]

While the exact binding coordination,[86] adsorption configurations,[45] and site requirements[83,87] associated with glucose isomerization to fructose and sorbose continue to be studied computationally and experimentally, the kinetic relevance of their respective hydride shift transition states can be experimentally detected through measurement of the H/D kinetic isotope effect (KIE).[42,82] KIE values reflect differences in the vibrational frequency and zero-point energy upon isotopic substitution of atoms in bonds that are broken along the reaction coordinate (derivation in Section S.3.2, Supporting Information). Deuteration of the alpha-carbon in glucose reactants results in measured glucose−fructose isomerization H/D KIE values of 2.1−2.3 (±0.2, 373 K) on both Ti-Beta-F and Ti-Beta-OH samples throughout the range of glucose concentrations studied here (0−50 wt % glucose). These values are consistent with theoretical H/D KIE values expected for transition state reaction coordinates involving C−H bond scissoring (~1500 cm^{-1}), consistent with the 1,2-hydride shift steps confirmed from isotopic tracer studies.[84,88] Measured KIE values of 2.1 also indicate that intrazeolitic transport artifacts do not corrupt measured rates, which would otherwise result in measurement of the square root of the theoretical KIE value (details in Section S.3.2, Supporting Information). Therefore, we conclude that the measured glucose−fructose isomerization rates reported here are uncorrupted by transport artifacts and reflect free energy differences between the kinetically relevant hydride shift transition state and the relevant adsorbed reactive intermediates. Next, we measure glucose isomerization turnover rates on a variety of Ti-Beta-F and Ti-Beta-OH samples and across a wide range of initial glucose concentrations, revealing the presence of different kinetic regimes that correspond to changes in reactive intermediate coverages.

3.3.2. Experimental Measurements of Glucose Isomerization Rate Constants on Hydrophobic and Hydrophilic Ti-Beta Zeolites. Initial glucose isomerization rates were collected on all Ti-Beta-F and Ti-Beta-OH samples at low glucose concentrations (1 wt %, 373 K), which correspond to a first-order kinetic regime in glucose concentration.[42] Apparent first-order glucose isomerization rate constants for fructose and sorbose formation are shown in parts A and B of Figure 4, respectively, as a function of total Ti content for all Ti-Beta samples studied here, and compared to data for Ti-Beta samples reported previously[42] (rate constants plotted as a function of Ti_{LA} per gram in Figure S.26, Supporting Information). On average, first-order rate constants are systematically higher (~6×) on Ti-Beta-F zeolites than on Ti-Beta-OH zeolites across a wide range of Ti content. First-order rate constants vary within ~3× among all Ti-Beta-F zeolites, and within ~2× among all Ti-Beta-OH zeolites, which are variations similar to those observed previously among Sn-Beta-F and Sn-Beta-OH zeolites of varying Sn content.[32] Furthermore, rate constants (per Ti) do not depend systematically on Ti content among Ti-Beta-F or Ti-Beta-OH zeolites, consistent with the absence of intracrystalline transport artifacts as expected from measured H/D KIE values of 2.1−2.3 (Section 3.3.1). Next, more detailed kinetic studies are performed on Ti-Beta-F-155 and Ti-Beta-OH-46, which are samples with kinetic behavior representative of the Ti-Beta-F and Ti-Beta-OH series, respectively.

Initial glucose isomerization rates were collected across a wide range of glucose concentrations (1−50 wt %) on both Ti-Beta-F-155 and Ti-Beta-OH-46. Thermodynamic activities for glucose and water are used here to describe rate data at high glucose concentrations due to expected nonideal solution behavior that affects reaction rates.[89] Nonideality was

DOI: 10.1021/jacs.8b08336
J. Am. Chem. Soc. 2018, 140, 14244−14266

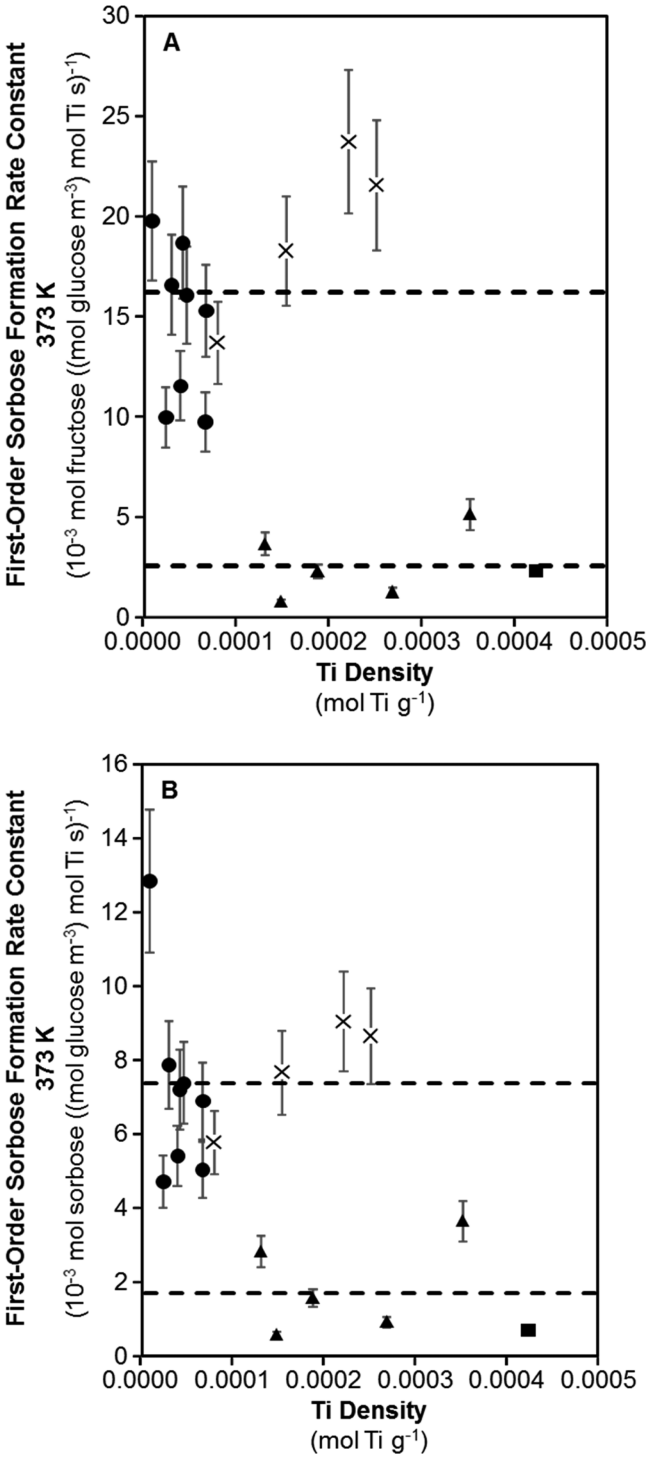

Figure 4. Initial first-order (a) fructose and (b) sorbose formation rates (373 K, pH 4) normalized per total Ti content as a function of Ti/Si ratio, for Ti-Beta-F (●) and Ti-Beta-OH samples (▲). Data on Ti-Beta-F (X) and Ti-Beta-OH (■) samples reported previously in ref 34 are plotted for comparison. Dashed lines correspond to average values within the series of Ti-Beta-F and Ti-Beta-OH samples.

accounted for using solution-phase activity coefficients (γ_i) which are unity under ideal conditions and diverge from unity at nondilute glucose concentrations. Activity coefficients for aqueous glucose solutions (1−52 wt %) reported at 298 K[90] were adjusted to reaction temperatures using the following equation (details in Section S.3.3, Supporting Information):[91]

$$\frac{-\bar{H}_i^{E}}{RT^2} = \frac{\delta}{\delta T}\ln \gamma_i \quad (5)$$

Here, $\bar{H}_i^{E}$ is the excess partial molar enthalpy of species i in solution and is assumed to be constant with temperature, R is the universal gas constant, and T is the absolute temperature in K. Activity coefficients approach unity ($\gamma_i \rightarrow 1$) as temperature increases or glucose concentrations decrease and solutions approach ideal behavior. Thermodynamic activities (a_i) for glucose (a_G) and water (a_W) were calculated using temperature-dependent and concentration-dependent activity coefficients according to the following equation:

$$a_i = \gamma_i \frac{c_i}{c^0} \quad (6)$$

where c^0 is the standard concentration (1 mol m^{-3}).

The dependence of initial fructose and sorbose formation rates (373 K, per Ti_{LA}) on the initial aqueous-phase glucose activity is shown in Figure 5 for Ti-Beta-F-155 and Ti-Beta-OH-46. Initial isomerization rates are 3−6× lower on Ti-Beta-OH-46 than on Ti-Beta-F-155 across the full range of a_G values studied, consistent with previously reported rates measured in dilute aqueous glucose solutions (0−1.5 wt %).[31] Initial glucose−fructose and glucose−sorbose isomerization rates on both Ti-Beta-F and Ti-Beta-OH zeolites show a first-order kinetic dependence on glucose activity at low a_G values (50−300 mol m^{-3}, ∼1−5 wt %, Figure 5 inset), consistent with previously reported glucose isomerization rates on Ti-Beta[42]

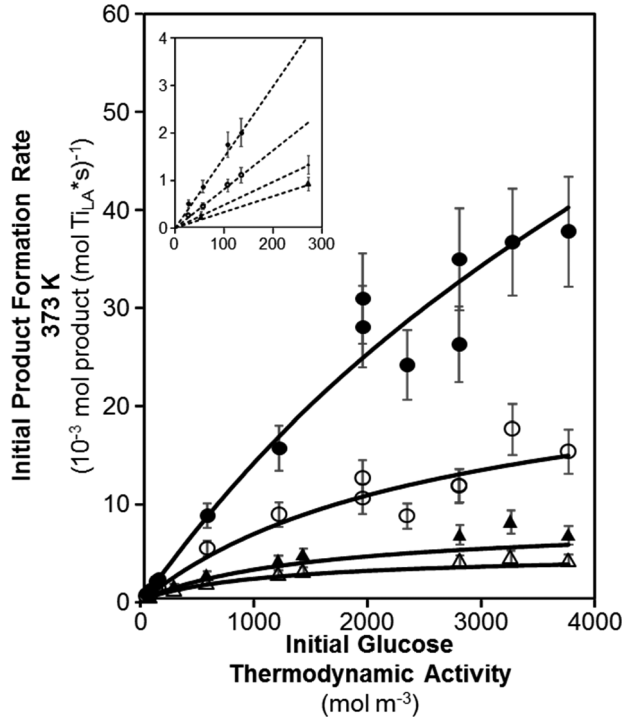

Figure 5. Dependence of initial glucose isomerization rates (373 K, pH 4) for fructose (filled) and sorbose (open) formation on Ti-Beta-F-155 (●, ○) and Ti-Beta-OH-46 (▲, △) as a function of initial glucose thermodynamic activity (corresponding to 1−50 wt % initial glucose concentration). Solid lines represent fits of the experimental data to the rate equation (eq 9) using activation enthalpies and entropies given in Table 4. The inset shows initial glucose isomerization rates at low glucose thermodynamic activities, highlighting the first-order kinetic regime.

DOI: 10.1021/jacs.8b08336
J. Am. Chem. Soc. 2018, 140, 14244−14266

and Sn-Beta[32] (isomerization rates shown as a function of glucose concentration in Figure S.27, Supporting Information). Glucose−fructose and glucose−sorbose isomerization rates become zero-order in a_G at high a_G values (>2700 mol m^{-3}), which is a kinetic regime that has not been previously reported to our knowledge for sugar isomerization on Lewis acidic zeolites. The onset of the zero-order kinetic regime in formation rates of both fructose and sorbose products, which are formed in parallel reaction pathways, are consistent with changes in the identities of the most abundant reactive intermediates at Lewis acid active sites and the fact that both products are formed at the same catalytic site.

Modeling multiple kinetic regimes requires consideration of at least two distinct coverage terms, only one of which is first-order in glucose thermodynamic activity, and suggests the presence of two distinct MARI species that are dependent on glucose activities. The general form of such a rate equation is

$$r_{isom} = \frac{k_{first} a_G}{1 + \frac{k_{first}}{k_{zero}} a_G} \quad (7)$$

In eq 7, r_{isom} is the initial glucose isomerization rate, k_{first} and k_{zero} are apparent first-order and zero-order rate constants, and a_G is the initial glucose thermodynamic activity. This rate equation simplifies to first-order and zero-order rate expressions at low and high a_G values, respectively. We next use spectroscopic techniques to characterize the nature of the bound intermediates as a function of glucose concentration in order to assign chemical significance to the first-order and zero-order kinetic regimes that are predicted by the generalized rate expression (eq 7).

3.4. Characterization of Active Site Complexes in First-Order and Zero-Order Kinetic Regimes. *3.4.1. Characterization of Bound Reactive Intermediates using ATR-IR and Modulation Excitation Spectroscopy.* The competitive adsorption of water solvent, glucose reactants, and glucose isomerization products within microporous voids and at Lewis acidic Ti sites in Ti-Beta-F-155 and Ti-Beta-OH-46 was probed in situ with ATR-IR and modulation excitation spectroscopy (MES). Figure 6A shows spectra corresponding to two independent intermediates extracted by phase-sensitive detection (PSD) and multicurve resolution-alternating least-squares analysis (MCR-ALS) from experiments with modulated glucose activities within the first-order kinetic regime (0−700 mol m^{-3}, 373 K) (time-resolved and phase-resolved spectra on Ti-Beta-F-155 shown in Figure S.28, Supporting Information). These spectra collected on both Ti-Beta-F-155 and Ti-Beta-OH-46 reflect the two independent reactive intermediates observed from interactions between solid surfaces and fluid phases composed of modulated glucose and water activities. One intermediate (Figure 6A, top) is characterized by water bending (δ(O−H) at 1630 cm^{-1})[92] and stretching (ν(O−H) around 3400 cm^{-1})[92] vibrations and lacks vibrational modes representative of glucose (ν(C−H) at 2900 cm^{-1};[93−95] concerted vibrations at 900−1500 cm^{-1}[93−96]), indicating that this intermediate is not derived from glucose. This species is the MARI; because it is not glucose-derived, spectra were normalized by the water bending resonance at 1630 cm^{-1} to facilitate comparison between samples in Figure 6A. The minor intermediate (Figure 6A, bottom) contains spectral features similar to vibrational modes of glucose and, thus, was normalized by the most intense glucose resonance (~1030 cm^{-1}). These features do not show significant

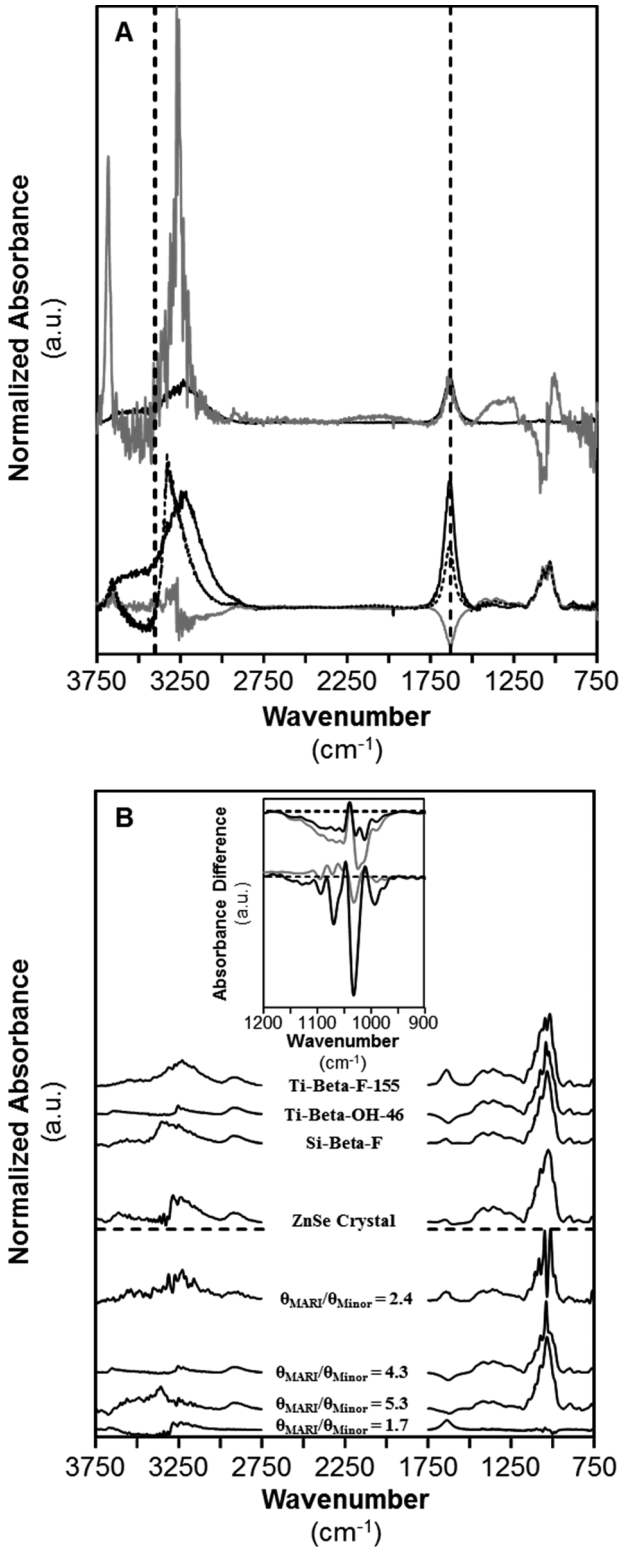

Figure 6. (a) ATR-IR spectra of MARI (top, water-derived) and minor (bottom, glucose-derived) intermediates on Ti-Beta-F-155 (black) and Ti-Beta-OH-46 (gray) that oscillate with aqueous-phase glucose activity (0−700 mol m^{-3}) at 373 K. Glucose spectra are normalized by the peak at ~1030 cm^{-1}, and water spectra are normalized by the peak at ~1630 cm^{-1}. Spectra reflecting aqueous-phase glucose (330 mol m^{-3}) flowing over the ZnSe crystal are overlaid on the glucose spectra (dashed). Dashed vertical lines at 1630 and 3400 cm^{-1} indicate water bending and stretching vibrational modes, respectively. (b) ATR-IR spectra of the MARI (bottom four)

DOI: 10.1021/jacs.8b08336
J. Am. Chem. Soc. 2018, 140, 14244−14266

Figure 6. continued

and minor (top four) species that oscillate with aqueous-phase glucose activity (~3000−3750 mol of glucose m^{-3}, 373 K, normalized by the maximum feature at ~1030 cm^{-1}) over Ti-Beta-F-155, Ti-Beta-OH-46, Si-Beta-F, and blank ZnSe crystal from top to bottom, respectively. The inset depicts difference spectra between aqueous-phase glucose flowing over the ZnSe crystal and the MARI (black) or minor species (gray) species observed on Ti-Beta-OH-46 (top) and Ti-Beta-F-155 (bottom) spectra from modulating aqueous-phase glucose activity (~3000−3750 mol of glucose m^{-3}) at 373 K after normalization by the peak centered at ~1030 cm^{-1}; dashed lines indicate the baseline. All spectra are obtained during MES experiments and isolated by processing through PSD and MCR-ALS.

differences from those of aqueous-phase glucose flowing over the ZnSe crystal (Figure 6A, bottom, dashed line), which suggests that such species are not coordinated to Lewis acidic Ti centers on Ti-Beta-F-155 and Ti-Beta-OH-46 and are likely solution-phase glucose. Together, the two species isolated from MES and sequential PSD and MCR-ALS during glucose concentration modulations at low activities (~0−700 mol m^{-3}) indicate that Ti-Beta zeolite surfaces bind a water-derived MARI species and a minor glucose species that is not coordinated to Lewis acid sites, supporting the mechanistic interpretations of first-order rate measurements at low a_G values.

Figure 6B shows spectra of the MARI species (bottom) and the minor intermediates (top) observed by MES at high glucose activities corresponding to zero-order kinetic regimes (~3000−3750 mol glucose m^{-3}) on Ti-Beta-F-155, Ti-Beta-OH-46, Si-Beta-F, and the ZnSe crystal. Spectral features between 900 to 1500 cm^{-1} in spectra of both the MARI and minor species reflect concerted ν(C−O), ν(C−C), δ(C−H), and δ(C−O−H)[93−97] vibrations of glucose-derived intermediates. Therefore, MARI and minor intermediates are assumed to be related oxygenate structures with identical molar extinction coefficients, such that their integrated areas correlate with their relative surface coverages with MARI species existing in higher abundances in MES experiments. Relative coverages between MARI and minor species are given in Table 3, indicating that MARI species are present at coverages that are 1.7−5.3× greater than the minority species.

Spectra of isolated species at high glucose activity modulations show relative changes in the quantities of water and glucose present on Ti-Beta-F-155 and Ti-Beta-OH-46 (Figure 6B), based on the relative intensities of vibrations from glucose-derived intermediates (ν(C−H) at 2900 cm^{-1}[93−95] and concerted vibrations between 900 and 1500 cm^{-1})[93−97]

Table 3. Relative Concentrations[a] of MARI and Minor Species during Modulation of Liquid-Phase Glucose Activity (~3000-3750 mol of glucose m^{-3}) at 373 K Followed by Processing by PSD and MCR-ALS

sample	relative concentration[a] ($\theta_{MARI}/\theta_{minor\ species}$)
Ti-Beta-F-155	2.4
Ti-Beta-OH-46	4.3
Si-Beta-F	5.3
ZnSe crystal	1.7

[a]Relative concentrations assume that the equivalent extinction coefficients for glucose vibrations at ~1030 cm^{-1} are between MARI and minor species.

and of the δ(O−H) water vibrations (1630 cm^{-1}).[92] In hydrophobic Ti-Beta-F-155, the intensity of spectral features attributed to glucose or glucose-derived intermediates (2900 cm^{-1};[93−95] 900−1500 cm^{-1}[93−97]) and the intensity of features attributed to water (1630 cm^{-1}) increase concomitantly, indicating that glucose adsorption into hydrophobic Beta pores facilitates coadsorption of water from its solvation sphere in bulk solution. This observation corroborates previous reports of coadsorption of water with glucose in both experimental measurements of adsorbed water and glucose content (using thermogravimetric analysis differential scanning calorimetry (TGA-DSC)) on Sn-Beta zeolites contacted with aqueous glucose solutions[31] and theoretical Gibbs ensemble Monte Carlo simulations of glucose adsorption from aqueous solutions within hydrophobic Si-Beta zeolites.[98] In contrast, spectra collected on Ti-Beta-OH-46 at identical glucose activities and temperatures show that water vibrational modes decrease as glucose vibrational modes increase, suggesting that glucose displaces water molecules previously adsorbed within hydrophilic Beta pores, consistent with the higher gas-phase water uptakes in hydrophilic versus hydrophobic materials (Section 3.2.2). The differences in relative water and glucose activities present within the hydrophilic and hydrophobic pores indicate that the hydrophobic nature of microporous voids in Beta affects the uptakes of both water and glucose molecules.

At high glucose activities, spectra observed on Ti-Beta-F-155 and Ti-Beta-OH-46 differ from those of the blank ZnSe crystal and Si-Beta-F, indicating that the MARI species on Ti-Beta materials do not reflect solution-phase glucose or physisorbed glucose and instead are glucose-derived intermediates coordinated to Lewis acidic Ti sites within Beta pores. The vibrational features of the MARI observed on Ti-Beta-F-155 at high glucose activities differ significantly from those on Ti-Beta-OH-46 (Figure 6B), particularly for ν(C−O), ν(C−C), δ(C−H), and δ(C−O−H) glucose vibrations (900−1200 cm^{-1}),[93−97] suggesting that glucose-derived reactive intermediates are structurally distinct on hydrophobic and hydrophilic Ti-Beta zeolites (additional discussion and DFT evidence on the likely and distinct adsorbate configurations are provided in Section S.4.2, Supporting Information). The inset of Figure 6B shows difference spectra for the two intermediates on each Ti-Beta sample relative to those for aqueous glucose on the ZnSe crystal, which show negative features at ~1030 cm^{-1} that may reflect ring-opened intermediates adsorbed at Ti sites in both Ti-Beta samples. DFT-calculated intermediates that form fructose and sorbose show the loss of the ~1030 cm^{-1} vibrational mode upon glucose ring opening (1029 and 1027 cm^{-1}, respectively); however, the ring-opened intermediate that forms sorbose contains a carbonyl group with a resonance at 1737 cm^{-1} (Movie S.2, Supporting Information) that is not present in any spectra measured on Ti-Beta-F-155 or Ti-Beta-OH-46 (Figure 6B). Thus, both the MARI and the minor species on Ti-Beta-F-155 and Ti-Beta-OH-46 likely react to form fructose, which may be expected given the higher selectivity toward fructose over sorbose on both Ti-Beta-F-155 and Ti-Beta-OH-46 at high glucose activities (Figures 5 and S.29, Supporting Information), yet hydrophobic and hydrophilic pore environments may stabilize different reactive intermediates.

The change in MARI and minor species on both hydrophobic and hydrophilic Ti-Beta samples detected during MES and isolated by PSD and MCR-ALS between low and

DOI: 10.1021/jacs.8b08336
J. Am. Chem. Soc. 2018, 140, 14244−14266

high glucose activities indicates that the MARI transitions from a water-derived to a glucose-derived intermediate bound to framework Ti atoms, consistent with measured glucose isomerization rates that transition from a first-order to a zero-order kinetic regime with increasing glucose thermodynamic activity (Figure 5). Further, the MARI species identified at high a_G values have distinct binding configurations on Ti-Beta-F and Ti-Beta-OH, which depend on the different solvating environments provided by silanol groups and coadsorbed water structures in hydrophobic and hydrophilic environments. Next, we use ex situ XAS to further characterize the structure of the adsorbed species on Ti-Beta observed after exposure to low and high glucose activities.

3.4.2. Ti Structural Characterization using XAS. To provide corroborating evidence for the predominant reactive intermediates proposed to exist at low and high glucose thermodynamic activity, we use XAS to determine Ti coordination numbers and Ti−O bond lengths in the presence and absence of adsorbed glucose intermediates. Apparent first-order isomerization rates measured at low glucose activities are consistent with dilute glucose coverages. EXAFS spectra collected on Ti-Beta-OH-46 (a sample with predominantly Lewis acidic Ti sites ($Ti_{LA}/Ti \approx 1$)) show that Ti sites are octahedrally coordinated at ambient temperature (CN = 6 ± 0.6, Table S.4 and Figures S.30−S.32, Supporting Information) and become tetrahedrally coordinated upon heating to 523 K in flowing helium (CN = 4 ± 0.4), consistent with previous reports on Ti-Beta[30] and the reversible adsorption of water to framework Ti sites upon exposure to ambient conditions. Ti−O bond lengths derived from EXAFS are similar to framework bond distances for dehydrated Lewis acid sites. The loss of two ligands upon heating reflects desorption of two water molecules from each Lewis acidic Ti site. UV−visible edge energies derived from Tauc plots also increase upon dehydration (523 K) by 0.22 eV on average (Table S.2 and Figure S.7, Supporting Information), indicative of octahedral to tetrahedral coordination changes of Ti sites. Similar findings from EXAFS spectra[99,100] and UV−visible edge energies[32] have been reported on Sn-Beta catalysts, in which the shift from octahedral to tetrahedral coordination upon dehydration is corroborated by ^{119}Sn NMR spectra that show the shift from octahedrally coordinated Sn resonances (685−700 ppm) to tetrahedral Sn resonances (425−445 ppm) upon dehydration at 423 K.[82,101] Thus, we conclude that apparent first-order kinetic regimes measured at low glucose activity correspond to glucose isomerization rates measured on Ti sites covered with two water molecules,[82,101] the most abundant reactive intermediate under these reaction conditions.[42]

Ex situ XANES spectra (Figures S.33 and S.34, Supporting Information) at ambient conditions most closely resemble octahedrally coordinated Ti sites (CN = 6, Table S.4, Supporting Information) on glucose-adsorbed Ti-Beta-OH-46. After dehydration treatments in flowing helium (523 K, 30 min), Ti sites became pentahedrally coordinated (CN = 5, Table S.4, Supporting Information), indicating the loss of one ligand per Ti site. This may reflect a change from bidentate to monodentate binding modes of glucose or desorption of one water molecule if glucose were originally bound in a monodentate fashion. The presence of pentahedrally coordinated Ti sites that persist after dehydration treatments would be consistent either with complete coverage of all Ti sites with a strongly bound intermediate (e.g., monodentate glucose) or with a mixture of sites in which some remain six-coordinate and populated by a strongly bound bidentate glucose intermediate and others revert to four-coordinate upon desorption of water ligands at 523 K. Although XAS cannot distinguish between these possibilities, the ATR-IR experiments show that Lewis acidic Ti sites in both Ti-Beta-OH-46 and Ti-Beta-F-155 are saturated with bound glucose intermediates at high glucose activities (>3000 mol m^{-3}) that are characteristic of the zero-order kinetic regime observed in Figure 5. Therefore, we propose that the octahedrally coordinated Ti sites observed after glucose adsorption reflect monodentate-bound glucose and one water ligand, and that the pentahedrally coordinated Ti sites observed after dehydration result from desorption of the water ligand.

Combining insights from in situ ATR-IR, ex situ XAS, and DFT calculations, we conclude that two different reactive species are dominant at low (~0−500 mol m^{-3}) and high glucose activities (>3000 mol m^{-3}). The most abundant reactive intermediates are two water molecules bound to Lewis acid centers at low glucose activities and bound glucose intermediates (in two different binding configurations) at high glucose activities. The bound glucose intermediates are distinct for Ti-Beta-F and Ti-Beta-OH, evidenced by shifts in IR peak centers and relative peak areas that are likely caused by the presence of extended solvent structures surrounding the adsorbed glucose.

3.5. Enthalpic and Entropic Consequences of Hydrophobic Reaction Pockets for Aqueous-Phase Glucose Isomerization. In this section, experimentally measured activation enthalpies and entropies on Ti-Beta-F and Ti-Beta-OH are compared with DFT-derived free energies to probe the consequences of intraporous silanol defects, and the coadsorbed water structures they stabilize, on aqueous-phase glucose isomerization catalysis.

3.5.1. Experimentally Determined Activation Enthalpies and Entropies. A reaction mechanism is shown in Scheme 1 depicting glucose isomerization pathways to fructose and to sorbose via quasi-equilibrated water adsorption and desorption, glucose adsorption, ring-opening, deprotonation, and the

Scheme 1. Plausible Glucose Isomerization Mechanism for Fructose and Sorbose Formation on Lewis Acidic Ti Sites[a]

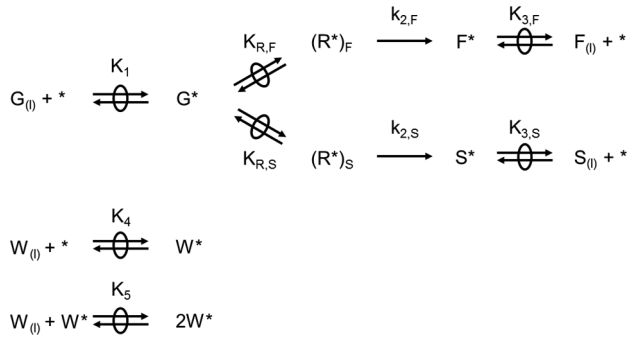

[a]Modified from ref 34 and shown in greater detail in Figures 3 and S.25, Supporting Information. Quasi-equilibrated glucose adsorption (step 1) forms reactive bound glucose intermediates (R^*_F and R^*_S), which form bound fructose (step 2a) or sorbose (step 2b) isomers through the formation of kinetically relevant hydride shift transition states. Quasi-equilibrated fructose (step 3,F) and sorbose (step 3,S) desorption phenomena release the product into the liquid phase. Quasi-equilibrated water adsorption onto Lewis acidic active sites (steps 4 and 5) inhibits isomerization rates at low glucose coverages.

DOI: 10.1021/jacs.8b08336
J. Am. Chem. Soc. 2018, 140, 14244−14266

kinetically relevant hydride shift steps, and is adapted from previously published work.[42] Having identified the dominant reactive intermediates at both low and high glucose thermodynamic activities in Section 3.4, the following rate equation can be derived from the mechanism in Scheme 1 to recover both first-order and zero-order dependences on glucose activity (complete derivation in Section S.5.1, Supporting Information):

$$r_i = \frac{K_1 K_{R,i} k_{2,i} \frac{a_G}{\gamma_{\ddagger,i}} (1 - \eta_i)}{\frac{K_4 K_5}{\gamma_{2W^*}} a_W{}^2 + \frac{K_1}{\gamma_{G^*}} a_G} \quad (8)$$

In eq 8, i stands for fructose or sorbose, K_1 is the lumped equilibrium constant for adsorbing glucose and forming the glucose-derived MARI at the tetrahedral Ti site, $K_{R,i}$ is the lumped equilibrium constant describing the formation of the structurally distinct intermediates that immediately precede fructose or sorbose formation from the glucose-derived MARI, $k_{2,i}$ is the rate constant for the kinetically relevant step that forms the hydride shift transition state from the relevant reactive intermediate, and K_4 and K_5 are equilibrium constants relating the sequential adsorption of two water molecules from the liquid phase to the Lewis acid site; all lumped rate and equilibrium constants in eq 8 are identified in Scheme 1. Additionally, η_i is the approach-to-equilibrium term, which is rigorously zero for initial isomerization rates extrapolated to zero conversion. Finally, γ_j is the activity coefficient of species j, where j denotes two bound water molecules (2W*), the bound glucose intermediate identified as MARI at high a_G values (G*), or the hydride shift transition states that form fructose and sorbose ($^{\ddagger},i$). This rate equation is the simplest kinetic model that satisfies the requirement of two relevant adsorbed intermediates and accounts for the nonideality of adsorbed or solution-phase species, which can be reduced to recover first-order and zero-order kinetic regimes at low and high glucose thermodynamic activities. These γ_j values approach unity for ideal solutions and ideal reactive intermediates, in which the ideality of adsorbed intermediates are typically defined as low-coverage and noninteracting species;[102] here, no such coadsorbate interactions are expected among glucose-derived species, and thus γ_j is assumed to be unity for adsorbed species.

Equation 8 can be recast in the following form, which was used to regress to initial fructose and sorbose rate data measured on Ti-Beta-F-155 and Ti-Beta-OH-46 as $a_G/a_W{}^2$ was varied:

$$r_i = \frac{\frac{K_1}{K_4 K_5} K_{R,i} k_{2,i} \frac{a_G}{a_W{}^2}}{1 + \frac{K_1}{K_4 K_5} \frac{a_G}{a_W{}^2}} \quad (9)$$

In eq 9, the apparent zero-order rate constant is defined as

$$k_{zero,i} = K_{R,i} k_{2,i} \quad (10)$$

which describes the formation of the kinetically relevant hydride shift transition states from the glucose-derived MARI species. Additionally, the competitive adsorption terms for glucose and water can be lumped together into a single apparent equilibrium constant,

$$K_{comp} = \frac{K_1}{K_4 K_5} \quad (11)$$

which describes the adsorption of glucose and concomitant displacement of two water molecules from the Ti site. These two values can be combined to define an apparent first-order rate constant,

$$k_{first,i} = k_{zero,i} K_{comp} = \frac{K_1 K_{R,i} k_{2,i}}{K_4 K_5} \quad (12)$$

which describes the formation of the kinetically relevant hydride shift transition state from aqueous-phase glucose and a pair of coadsorbed waters on the Ti site. Substituting eqs 10–12 into eq 9 yields the following equation, which follows a Langmuir–Hinshelwood formalism:

$$r_i = \frac{K_{comp} k_{zero,i} \frac{a_G}{a_W{}^2}}{1 + K_{comp} \frac{a_G}{a_W{}^2}} \quad (13)$$

Figure 7 shows initial fructose formation rates on Ti-Beta-F-155 as a function of glucose activity ($a_G \approx 50$–4000 mol m^{-3}),

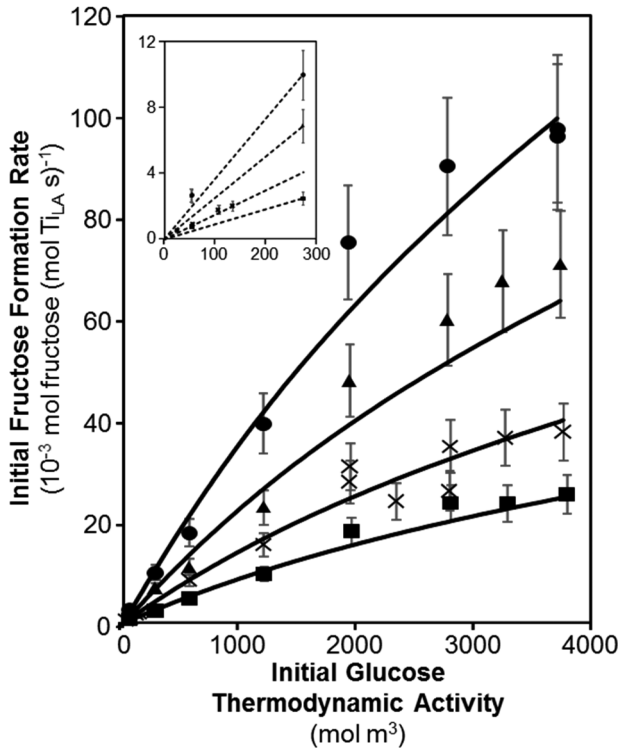

Figure 7. Dependence of initial fructose formation rates (pH 3) on Ti-Beta-F-155 on initial glucose thermodynamic activity (corresponding to 1–50 wt % glucose concentration) at 368 (■), 373 (X), 378 (▲), and 383 K (●). Solid lines represent regression of the data to the rate equation (eq 9) using activation enthalpies and entropies given in Table 4. The inset shows initial glucose isomerization rates at low glucose thermodynamic activities, highlighting the first-order kinetic regime.

water activity ($a_W \approx 40\,000$–$50\,000$ mol m^{-3}), and temperature (368–383 K), with similar plots of fructose formation rates on Ti-Beta-OH-46 and sorbose formation rates on both Ti-Beta-F-155 and Ti-Beta-OH-46 available in Figures S.35–S.37 (Supporting Information). We note that, while water solvent is typically considered to be in excess concentration, water activities vary by ~20% across the conditions studied here ($a_W \approx 40\,000$–$50\,000$ mol m^{-3}) and are accounted for using temperature-dependent activity

DOI: 10.1021/jacs.8b08336
J. Am. Chem. Soc. 2018, 140, 14244–14266

Table 4. Apparent Enthalpies and Entropies for First-Order and Zero-Order Rate Constants Describing Fructose and Sorbose Formation on Ti-Beta-F-155 and Ti-Beta-OH-46

	ΔH_{app} (kJ mol^{-1})		ΔS_{app} (J mol^{-1} K^{-1})		$\Delta\Delta H_{app}$ (kJ mol^{-1})	$\Delta\Delta S_{app}$ (J mol^{-1} K^{-1})	$\Delta\Delta G_{app}$ (kJ mol^{-1})
rate constant	Ti-Beta-F-155	Ti-Beta-OH-46	Ti-Beta-F-155	Ti-Beta-OH-46	(F−OH)[b]	(F−OH)[b]	(F−OH, 373 K)[b]
$k_{zero,fructose}$[a]	108 ± 10	86 ± 9	17 ± 26	−56 ± 25	22	73	−5
$k_{first,fructose}$	108	75	133	33	33	100	−4
$k_{zero,sorbose}$[a]	121 ± 7	93 ± 8	46 ± 19	−43 ± 20	28	89	−5
$k_{first,sorbose}$	121	82	162	46	39	116	−4
K_{comp}[a]	0 ± 0.5	−10 ± 0.5	116	89	11	27	1

[a]Errors correspond to 95% confidence intervals from regressions. Errors for first-order rate constants are not given as they reflect combined free energy differences for zero-order and competitive adsorption fits. [b]Differences in apparent activation enthalpies ($\Delta\Delta H_{app}$), entropies ($\Delta\Delta S_{app}$), and free energies ($\Delta\Delta G_{app}$ at 373 K) are listed as the difference between Ti-Beta-F-155 and Ti-Beta-OH-46.

coefficients and water concentrations following the same procedure used to calculate glucose activities (Section 3.3.2). Fructose and sorbose formation rates are plotted as a function of the relevant ratio of glucose and water activities (a_G/a_W^2) in Figures S.38 and S.39 (Supporting Information) at each temperature studied. Formation rates of both products on both Ti-Beta-F-155 and Ti-Beta-OH-46 show the kinetic behavior predicted by Langmuir−Hinshelwood formalisms (eq 13) with a first-order dependence at low a_G values (<500 mol m^{-3}) and an approximately zero-order dependence at high a_G values (>2700 mol m^{-3}).

Equations 10 and 11 can be rewritten in terms of apparent entropic and enthalpic contributions using the Eyring equation:

$$k_{zero,i} = \frac{k_B T}{h} e^{\Delta S^{\ddagger}_{zero,i}/R} e^{-\Delta H^{\ddagger}_{zero,i}/RT} \quad (14)$$

$$K_{comp} = e^{\Delta S_{comp}/R} e^{-\Delta H_{comp}/RT} \quad (15)$$

Here, k_B is the Boltzmann constant, h is Planck's constant, $\Delta S^{\ddagger}_{zero,i}$ and $\Delta H^{\ddagger}_{zero,i}$ are the apparent activation entropy and enthalpy of the hydride shift transition state referenced to the bound glucose MARI, and ΔS_{comp} and ΔH_{comp} are the apparent reaction entropy and enthalpy changes describing the competitive adsorption of glucose relative to water at the Lewis acid sites, respectively. We note that the temperature dependence of any nonunity activity coefficients for adsorbed species and transition state would be convoluted with the temperature dependences of enthalpy terms in eqs 14 and 15. Substitution of eqs 14 and 15 into eq 13 yields

$$r_i = \frac{k_B T}{h} \frac{e^{\Delta S^{\ddagger}_{zero,i}+\Delta S_{comp}/R} e^{-(\Delta H^{\ddagger}_{zero,i}+\Delta H_{comp})/RT} \frac{a_G}{a_W^2}}{1 + e^{\Delta S_{comp}/R} e^{-\Delta H_{comp}/RT} \frac{a_G}{a_W^2}} \quad (16)$$

Table 4 lists the apparent activation enthalpies and entropies obtained by regressing eq 16 to the experimental data for fructose and sorbose formation rates on Ti-Beta-F-155 and Ti-Beta-OH-46 (368−383 K, a_G = 50−4000, a_W = 40 000−50 000 mol m^{-3}; parity plots available in Figures S.40−S.43, Supporting Information). Apparent activation enthalpies for glucose−fructose isomerization on Ti-Beta-F-155 are identical (108 kJ mol^{-1}) for both first-order and zero-order rate constants, which measure differences in enthalpy between the same 1,2-hydride shift transition state and either two bound water molecules or a bound glucose intermediate on the Lewis acid site, respectively. Similarly, apparent activation enthalpies for the parallel glucose−sorbose isomerization reaction on Ti-Beta-F-155 are also identical (121 kJ mol^{-1}) for both first-order and zero-order rate constants. Together, these findings indicate that the competitive adsorption of glucose and two water molecules at Ti sites within low-defect Beta frameworks is isenthalpic and depends weakly on temperature in the range studied. This is consistent with glucose heats of adsorption calculated by theory (108 kJ mol^{-1})[98] that are approximately twice that of water heats of adsorption (~50 kJ mol^{-1}) measured by experiment from gravimetric and microcalorimetric studies on Ti-Beta-F.[30]

In contrast, apparent activation entropies for both glucose−fructose and glucose−sorbose isomerization on Ti-Beta-F-155 are ~120 J mol^{-1} K^{-1} larger for the first-order rate constant than for the zero-order rate constant. Zero-order activation entropies reflect differences between the relevant hydride shift transition state and the adsorbed glucose state, while first-order activation entropies reflect differences between the same transition state and a precursor state involving two adsorbed water molecules at the Lewis acid site and glucose in aqueous solution. As a result, differences in zero-order and first-order activation entropies reflect differences in the entropy of the precursor states describing adsorbed glucose (with two associated water molecules) or two adsorbed water molecules and aqueous-phase glucose. Therefore, the smaller apparent activation entropies measured in zero-order regimes reflect the losses in entropy upon exchange of two bound water molecules with bound glucose, likely dominated by the entropy losses upon glucose adsorption to active sites from aqueous phases. We note that similar apparent enthalpies and entropies are obtained from the first-order and zero-order rate constants modeled by eq 16 and from the Eyring equation from single rate measurements in the first-order (a_G = 275 mol m^{-3}) and zero-order (a_G ≈ 3500 mol m^{-3}) kinetic regimes, indicating that the data-fitting method used here does not significantly change the measured thermodynamic properties (Table S.5 and Figures S.44 and S.45, Supporting Information) or the conclusions derived from them.

Apparent activation enthalpies on Ti-Beta-OH-46 are also similar for the first-order and zero-order rate constants for glucose−fructose isomerization (75−86 kJ mol^{-1}, Table 4) and for glucose−sorbose isomerization (82−93 kJ mol^{-1}, Table 4). These data indicate that competitive adsorption of glucose and water onto Lewis acid sites within hydrophilic void environments also depends weakly on temperature in the range studied. Water adsorption has been reported to be ~7 kJ mol^{-1} more exothermic within Ti-Beta-OH than Ti-Beta-F from microcalorimetric studies,[30] presumably reflecting favorable hydrogen-bonding interactions with silanol defects, and similar effects of hydrogen-bonding interactions on the adsorption enthalpy of glucose seem reasonable. Indeed, the more

DOI: 10.1021/jacs.8b08336
J. Am. Chem. Soc. 2018, 140, 14244−14266

exothermic water adsorption enthalpies within hydrophilic channels of Ti-Beta-OH (by ~7 kJ mol^{-1}) resemble the lower apparent activation enthalpies (by 22−39 kJ mol^{-1}) for glucose−fructose isomerization on Ti-Beta-OH-46 than on Ti-Beta-F-155. As in the case for Ti-Beta-F, apparent activation entropies on Ti-Beta-OH-46 are ~100 J mol^{-1} K^{-1} higher for the apparent first-order rate constant than for the zero-order rate constant for both glucose−fructose and glucose−sorbose isomerization. These findings suggest that the polarity of the channel environment, and the associated coadsorbed water structures they may stabilize, affect the free energy changes associated with water and glucose competitive adsorption to similar extents. Further, DFT calculations with varying intraporous water (2−10 molecules) show scattered glucose adsorption enthalpies with increasing intraporous water content but do not show a strong increase or decrease in these values (Figure S.46A, Supporting Information), indicating that intraporous water has no systematic impact on glucose adsorption and water displacement (K_{comp}).

The kinetic effects of surrounding hydrophobic reaction pockets can be quantified from the differences in apparent activation enthalpies ($\Delta\Delta H$), entropies ($\Delta\Delta S$), and Gibbs free energies ($\Delta\Delta G$, 373 K) between Ti-Beta-F-155 and Ti-Beta-OH-46 for each parallel reaction (Table 4). For both glucose−fructose and glucose−sorbose isomerization, both first-order and zero-order apparent activation enthalpies are higher (22−39 kJ mol^{-1}) on Ti-Beta-F-155 than on Ti-Beta-OH-46, which seems reasonable for enthalpic stabilization of isomerization transition states by an additional hydrogen-bonding interaction with silanol groups (or coadsorbed water) present in more defective pore environments. Despite higher apparent activation enthalpies, initial isomerization rates are higher on Ti-Beta-F-155, reflecting greater apparent activation entropy gains (~85 J mol^{-1} K^{-1} for fructose, ~103 J mol^{-1} K^{-1} for sorbose) in both first-order and zero-order regimes. Similar findings have been observed for first-order glucose isomerization rates on Sn-Beta (373 K, 5 wt % glucose, per Sn), for which similar apparent activation energies but higher pre-exponential factors are measured on hydrophobic Sn-Beta-F than on hydrophilic Sn-Beta-OH,[87] although kinetic parameters measured in the first-order regime cannot be separated into individual contributions that affect competitive adsorption and hydride shift transition state formation from the bound glucose MARI species.

For both parallel reactions on Ti-Beta, $\Delta\Delta H$ and $\Delta\Delta S$ values are similar for both the first-order and zero-order rate constants, indicating that the dominant kinetic effect of the hydrophobic reaction pocket is the entropic stabilization of the hydride shift transition state relative to the bound glucose MARI and not of the bound water or glucose intermediates. For glucose isomerization reaction coordinates, descriptions of the hydride shift transition state include both the transitory glucose-derived complexes bound at Ti sites and the surrounding solvation environment provided by coadsorbed water molecules and confining lattice atoms. Solvent reorganization to form cavities near hydrophobic surfaces changes the hydrogen-bonding structure of water and can result in large entropy losses (~80 J mol^{-1} K^{-1}),[103] and similar entropy losses (>70 J mol^{-1} K^{-1}) have been observed as hydrophobic intermediates became more hydrophilic in nature at transition states for the catalytic formation of H_2O_2 on silica-supported Pd clusters.[104] We surmise that the similar (~85−103 J mol^{-1} K^{-1}) entropy differences measured here for glucose isomerization in Ti-Beta-F and Ti-Beta-OH suggest reorganization of solvating water shells between the kinetically relevant precursor and transition states, given that both water- and glucose-derived moieties are hydrophilic and able to hydrogen bond with the solvating environment. Further, because the stability of the transition state relative to the bound glucose MARI species affects both first-order and zero-order rate constants, comparison between first-order and zero-order rate constants (Table 4) indicates that hydrophobic surrounding environments have a weaker effect on water and glucose competitive adsorption equilibrium constants and a predominant effect on the stability of kinetically relevant hydride shift transition states relative to the bound glucose MARI species.

In summary, experimental kinetic measurements indicate that the dominant effect of hydrophobic voids in Ti-Beta-F is the entropic stabilization of the hydride shift transition state relative to bound glucose MARI species ($\Delta\Delta H$ and $\Delta\Delta S$ values for k_{zero}, Table 4) and not the competitive adsorption of water and glucose ($\Delta\Delta H$ and $\Delta\Delta S$ values for K_{comp} near zero, Table 4). As a result, isomerization turnover rates measured in both first-order and zero-order kinetic regimes (per Ti_{LA}) are higher (by similar factors) when active Ti sites are confined within hydrophobic than hydrophilic voids. Small enthalpic penalties for confining transition states within hydrophobic voids of Ti-Beta-F are compensated by significantly more favorable entropic gains, resulting in higher rate constants than on hydrophilic Ti-Beta-OH. This entropic stabilization of the transition state relative to the adsorbed glucose intermediate is the dominant kinetic effect of confining glucose isomerization reaction coordinates within hydrophobic reaction pockets. In what follows, we assess the effects of hydrophobic and hydrophilic reaction environments on glucose isomerization using DFT calculations that consider the effects of additional water molecules present in reaction environments on glucose isomerization free energy landscapes. These calculations focus primarily on the effects of coadsorbed water on the stability of the hydride shift transition state, relative to the adsorbed glucose intermediate observed from ATR-IR spectra at high a_G values.

3.5.2. DFT-Derived Activation Enthalpies and Entropies. The kinetic effects of coadsorbed water on glucose−fructose isomerization were examined by changing the number of intraporous water molecules (2−10) that interact with the transition state for the 1,2-hydride shift step, the adsorbed glucose state, and the desorbed glucose state (the closed Ti site without any organic species present) individually. Additional kinetic effects from proximal silanol groups that may exist in Ti-Beta-OH materials are possible but cannot be quantified appropriately without more precise definitions of active Ti site structures (e.g., closed, open), which is the subject of ongoing work. Alterations in the nature (e.g., closed, open) of Lewis acidic Sn sites may significantly affect glucose−fructose isomerization activation enthalpies;[45] however, the similar activation enthalpies measured experimentally on Ti-Beta-F and Ti-Beta-OH (Table 4) do not suggest that such dramatic differences prevail among active Ti site structures in hydrophobic and hydrophilic Ti-Beta zeolites. Therefore, to isolate the kinetic roles of coadsorbed water molecules on the stability of hydride shift transition states, the active site model was restricted to a closed Ti site without proximal silanol defects.

The positions of water molecules in these studies were determined by first fully solvating three cases: the 1,2-hydride

DOI: 10.1021/jacs.8b08336
J. Am. Chem. Soc. 2018, 140, 14244−14266

shift transition state, the adsorbed ring-closed glucose state, and the closed Ti site with a proximal, partially bound water cluster. Water was systematically removed from each position in these clusters to determine the most weakly bound water molecule, which was then used as the basis for each subsequent water removal. For example, starting with 10 water molecules solvating the 1,2-hydride shift transition state, each individual water molecule was removed to create 10 distinct 9-water arrangements, each of which was optimized into its lowest free energy configuration. The 9-water configuration with the lowest free energy was used to generate 9 distinct 8-water arrangements prior to energy minimization, a process that was repeated until no water molecules remained. The arrangement of water molecules at each discrete water density on the 1,2-hydride shift transition state, the adsorbed glucose state, and the closed Ti site corresponding to the lowest free energy was then used to calculate enthalpy and entropy barriers for the apparent first-order and zero-order rate constants.

The aqueous nature of these reactions prohibits direct assessment of how many water molecules adsorb or desorb over the course of the reaction within hydrophobic and hydrophilic environments. ATR-IR experiments confirm prior reports that glucose adsorption entrains some number of water molecules into hydrophobic channels[31,98] and indicates that glucose displaces some number of water molecules upon adsorption within hydrophilic channels. Despite these apparent shifts in intraporous water content upon glucose adsorption, K_{comp} values are nearly identical in Ti-Beta-F and Ti-Beta-OH materials, which correspond to the adsorption of glucose and concomitant desorption of two water molecules. Therefore, the difference in reactivity between Ti-Beta-F and Ti-Beta-OH is directly attributable to changes in the zero-order apparent rate constants, which reflect differences in free energy between hydride shift transition states and the adsorbed glucose MARI state. This reaction event likely causes net-zero changes in the amount of coadsorbed water within either material.

DFT-predicted apparent zero-order activation enthalpies systematically increase from 165 to 276 kJ mol^{-1} and apparent zero-order activation entropies systematically increase from −12 to 49 J mol^{-1} K^{-1} as the coadsorbed water density increases from 2−10 molecules (Figure S.46C, Supporting Information). Similar increases in apparent activation enthalpies and entropies with increasing intraporous water content were observed for the first-order regime (Figure S.46B, Supporting Information). These DFT-predicted trends, however, directly contradict the decrease in experimentally measured activation enthalpies ($\Delta\Delta H_{zero,fructose}$ of 22 kJ mol^{-1}) and large decrease in entropies ($\Delta\Delta S_{zero,fructose}$ of 73 J mol^{-1} K^{-1}) on Ti-Beta-OH-46 compared to Ti-Beta-F-155 (Table 4) in the zero-order regime.

The inability to directly quantify the water content within the pores prohibits quantitative comparisons between DFT and experiments. Despite overall trends that suggest an increase in activation enthalpy with increasing intraporous water density, certain changes in water content produce statistically insignificant changes in activation enthalpies, such as the shift from 2 to 4 intraporous water molecules that results in a slight decrease in the zero-order activation enthalpy from 165 to 155 kJ mol^{-1}, or the shift from 5 to 7 intraporous water molecules that results in a slight increase in the activation enthalpy from 209 to 214 kJ mol^{-1}. The overall results from DFT, however, indicate that large increases in the amount of water that directly solvates glucose-derived species cause an increase in activation enthalpies and entropies, suggesting that such large changes are unlikely between hydrophobic and hydrophilic materials. Further, this suggests that adsorbed glucose species may be sufficiently solvated within Ti-Beta-F because of water molecules entrained upon glucose adsorption and the desorbed waters from the Lewis acid site, as well as that the increase in intraporous water content at other regions within zeolitic voids has little impact on activation enthalpies.

The significant decrease in activation entropy between Ti-Beta-F and Ti-Beta-OH ($\Delta\Delta S_{zero,fructose}$ of 73 J mol^{-1} K^{-1}) demonstrates that intraporous water must have an impact on these reactions without a concomitant impact on activation enthalpy, which perhaps indicates that these effects are caused by alterations in the second-layer solvation shell around glucose-derived intermediates. In other words, glucose adsorption into hydrophobic materials entrains sufficient water molecules to directly solvate itself and the 1,2-hydride shift transition state that forms fructose, yet these materials lack extended water structures otherwise present in defect-laden hydrophilic materials that restrict the mobility of the first solvation shell of glucose. The net result is a decrease in the entropy of the 1,2-hydride shift transition state, reflected in a decrease in both first-order and zero-order activation entropies on Ti-Beta-OH. Although the DFT results and entropy treatments used here do not provide straightforward explanations of the experimental findings, they do appear to capture broader effects of intraporous water that can be used to eliminate some possible hypotheses that would otherwise be difficult to assess without DFT. We note that more accurate modeling of this solvated reaction coordinate, using ab initio molecular dynamics simulations, may be warranted in future efforts that intend to more closely connect with experimental findings.

4. CONCLUSIONS

The confinement of binding sites within hydrophobic or hydrophilic micropore environments influences turnover rates of aqueous-phase reactions through effects on the competitive adsorption of solvent and reactant molecules at binding sites, as well as on the structures of solvent clusters and networks within void spaces that influence Gibbs free energies of transition states and kinetically relevant reactive intermediates. These effects were studied here using aqueous-phase glucose isomerization to fructose and sorbose on Ti-Beta samples comprising varying contents (by 10×) of isolated, active Lewis acidic Ti sites that were synthesized directly or modified post-synthetically in order to obtain suites of materials that confined such sites within hydrophobic (Ti-Beta-F) and hydrophilic (Ti-Beta-OH) frameworks of widely varying residual silanol defect density (by 100×). Hydrophilic Ti-Beta-OH samples adsorbed 20−25× higher amounts of water (P/P_0 = 0−0.2, 293 K) than hydrophobic Ti-Beta-F samples and stabilized water in structures characterized by increased extents of hydrogen-bonded networks versus the gas-like molecular structures present within hydrophobic micropores. Initial glucose−fructose and glucose−sorbose isomerization turnover rates (368−383 K, per Ti_{LA}) are first-order at dilute glucose thermodynamic activities (a_G = 50−300 mol m^{-3}) and become zero-order at high glucose thermodynamic activities (a_G = 2700−4000 mol m^{-3}), reflecting a change in the MARI at Ti sites from two bound water ligands to adsorbed glucose-derived intermediates. These changes in the identity of the MARI with increasing glucose thermodynamic activity are

DOI: 10.1021/jacs.8b08336
J. Am. Chem. Soc. 2018, 140, 14244−14266

consistent with shifts in Ti coordination from XANES spectra and are confirmed by spectral identification of intermediate structures using modulation excitation spectroscopy during ATR-IR experiments.

The measurement of first-order and zero-order kinetic behavior enables decoupling the kinetic effects of glucose and water competitive adsorption at active Ti sites from those of kinetically relevant isomerization transition state stabilization to assess the effects of hydrophilic and hydrophobic reaction environments on adsorption and catalytic phenomena independently. Glucose isomerization rates were ~6× higher (368−383 K, per Ti_{LA}) on Ti-Beta-F than on Ti-Beta-OH in both first-order and zero-order kinetic regimes, reflecting both competitive adsorption constants between two waters and one glucose at Ti sites that are essentially insensitive to the polarity of confining reaction environments and Gibbs free energy differences of kinetically relevant hydride shift transition states relative to their bound glucose precursors that are significantly lower within hydrophobic environments. Lower zero-order activation enthalpies and entropies measured on Ti-Beta-OH versus on Ti-Beta-F reflect the effects of higher coadsorbed water and silanol defect densities that cause modest enthalpic stabilization by hydrogen bonding but more severe entropic destabilization of isomerization transition states. Insights from DFT suggest that glucose is solvated within the hydrophobic micropores characteristic of Ti-Beta-F from water molecules entrained upon sugar adsorption and those desorbed from active Ti sites upon formation of ring-opened sugar intermediates; however, the higher water densities present within hydrophilic environments characteristic of Ti-Beta-OH interact with the hydride shift transition state, leading to entropic destabilization.

The experimental and theoretical data presented herein provide evidence that silanol defects and associated coadsorbed water within the microporous reaction pockets of zeolites mediate entropy−enthalpy compromises that influence Gibbs free energies of kinetically relevant glucose isomerization transition states. Similar entropy−enthalpy compromises have also been observed within metalloenzyme reaction pockets.[4,105] For example, freeze-trapping X-ray crystallography studies of D-xylose isomerase have shown the migration of water molecules during protein folding and throughout the glucose−fructose isomerization pathway to assist proton-shuttling events involved in glucose ring-opening and hydride shift steps.[4] Coadsorbed water is not expelled from the reaction pocket in D-xylose isomerase and continues to interact with bound intermediates, reminiscent of the entrainment of water molecules with glucose upon adsorption within hydrophobic zeolite pores and the influence of such coadsorbed water to mediate entropy−enthalpy compromises in determining intermediate and transition state stability.

These findings indicate that aqueous-phase sugar isomerization turnover rates on hydrophobic and hydrophilic zeolites are sensitive to the presence of coadsorbed solvent molecules within the reaction environment. As a result, the density and location of intraporous silanol defects in zeolites, which depend on their synthetic and post-synthetic treatment history, are structural features that influence catalytic rates because they determine the amount and structure of coadsorbed solvent molecules, clusters, and extended networks within reaction environments. The in situ and ex situ IR characterization techniques described here are particularly useful for quantifying active site and hydrophilic defect densities, as well as for probing water structures within hydrophobic and hydrophilic confining environments under both gas-phase and liquid-phase conditions. More accurate modeling of coadsorbed solvent densities within low-defect and high-defect porous structures promises to help establish stronger connections between computational and experimental studies. While the polarity of confining environments around binding sites in zeolites has been recognized to influence turnover rates in aqueous-phase catalysis, including several cases for which rate acceleration within hydrophobic confining environments reflect adsorption phenomena, the findings presented herein document an example of rate acceleration that predominantly reflects the influence of hydrophobic confining environments on transition state stability.

■ ASSOCIATED CONTENT

Supporting Information

The Supporting Information is available free of charge on the ACS Publications website at DOI: 10.1021/jacs.8b08336.

Movies showing vibrational modes of fructose and sorbose from DFT models (ZIP)

XRD patterns, adsorption isotherms, SEM images, UV−vis spectra and Tauc plots, IR spectra after either CD_3CN or pyridine titration, IR spectra during gas-phase water flow experiments, ^{13}NMR spectra, sorbose free energy diagram and associated mechanism, kinetic isotope effect derivation, additional plots showing initial glucose isomerization rates as a function of Lewis acid site density, additional ATR-IR MES PSD MCR-ALS processing details and example spectra, XAS spectra and fitting details, additional rate expressions and associated derivations, additional plots of fructose and sorbose rates as a function of temperature and associated parity plots for model regressions, additional data fitting methods and Arrhenius plots for first-order and zero-order rate constants, and computational enthalpy, entropy, and free energy measurements as a function of coadsorbed water density (PDF)

■ AUTHOR INFORMATION

Corresponding Author

*rgounder@purdue.edu

ORCID

James W. Harris: 0000-0001-6760-9951
Jason S. Bates: 0000-0002-7603-9687
Megan E. Witzke: 0000-0003-1204-6711
Jeffrey T. Miller: 0000-0002-6269-0620
David W. Flaherty: 0000-0002-0567-8481
David D. Hibbitts: 0000-0001-8606-7000
Rajamani Gounder: 0000-0003-1347-534X

Notes

The authors declare no competing financial interest.

■ ACKNOWLEDGMENTS

M.J.C., J.W.H., J.C.V.V., J.S.B., and R.G. gratefully acknowledge financial support provided by the Purdue Process Safety and Assurance Center (P2SAC) and the Ralph W. and Grace M. Showalter Research Trust, and Jacklyn Hall and Alyssa LaRue for assistance with NMR studies. E.C.W and J.T.M. acknowledge support by the National Science Foundation under Cooperative Agreement no. EEC-1647722. Use of the

DOI: 10.1021/jacs.8b08336
J. Am. Chem. Soc. 2018, 140, 14244−14266

Advanced Photon Source was supported by the U.S. Department of Energy, Office of Basic Energy Sciences, under Contract no. DE-AC02-06CH11357. MR-CAT operations are supported by the Department of Energy and the MRCAT member institutions. M.G., S.K., and D.D.H. acknowledge the Extreme Science and Engineering Discovery Environment (XSEDE) through allocation CTS160041; XSEDE is supported by National Science Foundation Grant no. ACI-1548562. D.W.F. and M.E.W. acknowledge financial support from the National Science Foundation (CBET-15531377), a National Science Foundation Graduate Research Fellowship Program (DGE-1144245), and the TechnipFMC Educational Fund Fellowship at the University of Illinois. They also thank Pranjali Priyadarshini for developing the apparatus and analysis for the MES-PSD experiments.

REFERENCES

(1) Berg, J. M.; Tymoczko, J. L.; Stryer, L. *Biochemistry*, 2002 ed.; W. H. Freeman: New York, 2002.
(2) Snyder, P. W.; Lockett, M. R.; Moustakas, D. T.; Whitesides, G. M. Is it the shape of the cavity, or the shape of the water in the cavity? *Eur. Phys. J.: Spec. Top.* **2014**, *223* (5), 853−891.
(3) Lemieux, R. U. How Water Provides the Impetus for Molecular Recognition in Aqueous Solution. *Acc. Chem. Res.* **1996**, *29* (8), 373−380.
(4) Kovalevsky, A. Y.; Hanson, L.; Fisher, S. Z.; Mustyakimov, M.; Mason, S. A.; Forsyth, V. T.; Blakeley, M. P.; Keen, D. A.; Wagner, T.; Carrell, H. L.; Katz, A. K.; Glusker, J. P.; Langan, P. Metal Ion Roles and the Movement of Hydrogen during Reaction Catalyzed by D-Xylose Isomerase: A Joint X-Ray and Neutron Diffraction Study. *Structure* **2010**, *18* (6), 688−699.
(5) Olsson, T. S. G.; Ladbury, J. E.; Pitt, W. R.; Williams, M. A. Extent of enthalpy-entropy compensation in protein-ligand interactions. *Protein Sci.* **2011**, *20* (9), 1607−1618.
(6) Kauzmann, W. Some Factors in the Interpretation of Protein Denaturation. *Adv. Protein Chem.* **1959**, *14*, 1−63.
(7) Breiten, B.; Lockett, M. R.; Sherman, W.; Fujita, S.; Al-Sayah, M.; Lange, H.; Bowers, C. M.; Heroux, A.; Krilov, G.; Whitesides, G. M. Water Networks Contribute to Enthalpy/Entropy Compensation in Protein-Ligand Binding. *J. Am. Chem. Soc.* **2013**, *135* (41), 15579−15584.
(8) Schrader, A. M.; Monroe, J. I.; Sheil, R.; Dobbs, H. A.; Keller, T. J.; Li, Y. X.; Jain, S.; Shell, M. S.; Israelachvili, J. N.; Han, S. G. Surface chemical heterogeneity modulates silica surface hydration. *Proc. Natl. Acad. Sci. U. S. A.* **2018**, *115* (12), 2890−2895.
(9) Ohba, T. Size-Dependent Water Structures in Carbon Nanotubes. *Angew. Chem., Int. Ed.* **2014**, *53* (31), 8032−8036.
(10) Giovambattista, N.; Debenedetti, P. G.; Rossky, P. J. Hydration Behavior under Confinement by Nanoscale Surfaces with Patterned Hydrophobicity and Hydrophilicity. *J. Phys. Chem. C* **2007**, *111* (3), 1323−1332.
(11) Chakraborty, S.; Kumar, H.; Dasgupta, C.; Maiti, P. K. Confined Water: Structure, Dynamics, and Thermodynamics. *Acc. Chem. Res.* **2017**, *50* (9), 2139−2146.
(12) Majumder, M.; Chopra, N.; Andrews, R.; Hinds, B. J. Enhanced flow in carbon nanotubes. *Nature* **2005**, *438*, 44.
(13) Holt, J. K.; Park, H. G.; Wang, Y.; Stadermann, M.; Artyukhin, A. B.; Grigoropoulos, C. P.; Noy, A.; Bakajin, O. Fast mass transport through sub-2-nanometer carbon nanotubes. *Science* **2006**, *312* (5776), 1034−1037.
(14) Dalla Bernardina, S.; Paineau, E.; Brubach, J. B.; Judeinstein, P.; Rouziere, S.; Launois, P.; Roy, P. Water in Carbon Nanotubes: The Peculiar Hydrogen Bond Network Revealed by Infrared Spectroscopy. *J. Am. Chem. Soc.* **2016**, *138* (33), 10437−10443.
(15) Mellmer, M. A.; Sener, C.; Gallo, J. M. R.; Luterbacher, J. S.; Alonso, D. M.; Dumesic, J. A. Solvent Effects in Acid-Catalyzed Biomass Conversion Reactions. *Angew. Chem., Int. Ed.* **2014**, *53* (44), 11872−11875.
(16) Liu, Y.; Vjunov, A.; Shi, H.; Eckstein, S.; Camaioni, D. M.; Mei, D.; Baráth, E.; Lercher, J. A. Enhancing the catalytic activity of hydronium ions through constrained environments. *Nat. Commun.* **2017**, *8*, 14113.
(17) Iler, R. K. *The Chemistry of Silica: Solubility, Polymerization, Colloid and Surface Properties and Biochemistry of Silica*; Wiley: New York, 1979.
(18) Vinogradova, O. I. Drainage of a Thin Liquid-Film Confined Between Hydrophobic Surfaces. *Langmuir* **1995**, *11* (6), 2213−2220.
(19) Bonaccurso, E.; Butt, H. J.; Craig, V. S. J. Surface roughness and hydrodynamic boundary slip of a newtonian fluid in a completely wetting system. *Phys. Rev. Lett.* **2003**, *90* (14), 144501.
(20) Vinogradova, O. I.; Bunkin, N. F.; Churaev, N. V.; Kiseleva, O. A.; Lobeyev, A. V.; Ninham, B. W. Submicrocavity Structure of Water Between Hydrophobic and Hydrophilic Walls as Revealed by Optical Cavitation. *J. Colloid Interface Sci.* **1995**, *173* (2), 443−447.
(21) Shantz, D. F.; Schmedt auf der Gunne, J.; Koller, H.; Lobo, R. F. Multiple-Quantum 1H MAS NMR Studies of Defect Sites in As-Made All-Silica ZSM-12 Zeolite. *J. Am. Chem. Soc.* **2000**, *122* (28), 6659−6663.
(22) Shantz, D. F.; Fild, C.; Koller, H.; Lobo, R. F. Guest-Host Interactions in As-Made Al-ZSM-12: Implications for the Synthesis of Zeolite Catalysts. *J. Phys. Chem. B* **1999**, *103* (49), 10858−10865.
(23) Koller, H.; Lobo, R. F.; Burkett, S. L.; Davis, M. E. SiO- HOSi Hydrogen Bonds in As-Synthesized High-Silica Zeolites. *J. Phys. Chem.* **1995**, *99* (33), 12588−12596.
(24) Axon, S. A.; Klinowski, J. Synthesis and characterization of defect-free crystals of MFI-type zeolites. *Appl. Catal., A* **1992**, *81* (1), 27−34.
(25) Chezeau, J. M.; Delmotte, L.; Guth, J. L.; Soulard, M. High-Resolution Solid-State Si-29 and C-13 NMR on Highly Siliceous MFI-Type Zeolites Synthesized in Nonalkaline Fluoride Medium. *Zeolites* **1989**, *9* (1), 78−80.
(26) Dapsens, P. Y.; Mondelli, C.; Jagielski, J.; Hauert, R.; Perez-Ramirez, J. Hierarchical Sn-MFI zeolites prepared by facile top-down methods for sugar isomerisation. *Catal. Sci. Technol.* **2014**, *4* (8), 2302−2311.
(27) Zhang, L.; Chen, K. Z.; Chen, B. H.; White, J. L.; Resasco, D. E. Factors that Determine Zeolite Stability in Hot Liquid Water. *J. Am. Chem. Soc.* **2015**, *137* (36), 11810−11819.
(28) Lami, E. B.; Fajula, F.; Anglerot, D.; Des Courieres, T. Single-Step Dealumination of Zeolite-Beta Precursors for the Preparation of Hydrophobic Adsorbents. *Microporous Mater.* **1993**, *1* (4), 237−245.
(29) Deruiter, R.; Kentgens, A. P. M.; Grootendorst, J.; Jansen, J. C.; Vanbekkum, H. Calcination and Deboronation of B-MFI Single-Crystals. *Zeolites* **1993**, *13* (2), 128−138.
(30) Blasco, T.; Camblor, M. A.; Corma, A.; Esteve, P.; Guil, J. M.; Martinez, A.; Perdigon-Melon, J. A.; Valencia, S. Direct Synthesis and Characterization of Hydrophobic Aluminum-Free Ti-Beta Zeolite. *J. Phys. Chem. B* **1998**, *102* (1), 75−88.
(31) Gounder, R.; Davis, M. E. Beyond Shape Selective Catalysis with Zeolites: Hydrophobic Void Spaces in Zeolites Enable Catalysis in Liquid Water. *AIChE J.* **2013**, *59* (9), 3349−3358.
(32) Harris, J. W.; Cordon, M. J.; Di Iorio, J. R.; Vega-Vila, J. C.; Ribeiro, F. H.; Gounder, R. Titration and quantification of open and closed Lewis acid sites in Sn-Beta zeolites that catalyze glucose isomerization. *J. Catal.* **2016**, *335*, 141−154.
(33) Mei, D. H.; Lercher, J. A. Mechanistic Insights into Aqueous Phase Propanol Dehydration in H-ZSM-5 Zeolite. *AIChE J.* **2017**, *63* (1), 172−184.
(34) Khouw, C. B.; Dartt, C. B.; Labinger, J. A.; Davis, M. E. Studies on the Catalytic Oxidation of Alkanes and Alkenes by Titanium Silicates. *J. Catal.* **1994**, *149* (1), 195−205.
(35) Grosso-Giordano, N. A.; Schroeder, C.; Okrut, A.; Solovyov, A.; Schöttle, C.; Chassé, W.; Marinković, N.; Koller, H.; Zones, S. I.; Katz, A. Outer-Sphere Control of Catalysis on Surfaces: A Comparative Study of Ti(IV) Single-Sites Grafted on Amorphous

DOI: 10.1021/jacs.8b08336
J. Am. Chem. Soc. 2018, 140, 14244−14266

versus Crystalline Silicates for Alkene Epoxidation. *J. Am. Chem. Soc.* **2018**, *140* (15), 4956−4960.
(36) Zapata, P. A.; Faria, J.; Ruiz, M. P.; Jentoft, R. E.; Resasco, D. E. Hydrophobic Zeolites for Biofuel Upgrading Reactions at the Liquid-Liquid Interface in Water/Oil Emulsions. *J. Am. Chem. Soc.* **2012**, *134* (20), 8570−8578.
(37) Zapata, P. A.; Huang, Y.; Gonzalez-Borja, M. A.; Resasco, D. E. Silylated hydrophobic zeolites with enhanced tolerance to hot liquid water. *J. Catal.* **2013**, *308*, 82−97.
(38) Zhao, H.; Yokoi, T.; Kondo, J. N.; Tatsumi, T. Hydrophobicity enhancement of Ti-MWW catalyst and its improvement in oxidation activity. *Appl. Catal., A* **2015**, *503*, 156−164.
(39) Lewis, J. D.; Van de Vyver, S.; Crisci, A. J.; Gunther, W. R.; Michaelis, V. K.; Griffin, R. G.; Roman-Leshkov, Y. A Continuous Flow Strategy for the Coupled Transfer Hydrogenation and Etherification of 5-(Hydroxymethyl)furfural using Lewis Acid Zeolites. *ChemSusChem* **2014**, *7* (8), 2255−2265.
(40) Bukowski, B. C.; Bates, J. S.; Gounder, R.; Greeley, J. First principles, microkinetic, and experimental analysis of Lewis acid site speciation during ethanol dehydration on Sn-Beta zeolites. *J. Catal.* **2018**, *365*, 261−276.
(41) Bates, J. S.; Gounder, R. Influence of confining environment polarity on ethanol dehydration catalysis by Lewis acid zeolites. *J. Catal.* **2018**, *365*, 213−226.
(42) Gounder, R.; Davis, M. E. Monosaccharide and disaccharide isomerization over Lewis acid sites in hydrophobic and hydrophilic molecular sieves. *J. Catal.* **2013**, *308*, 176−188.
(43) van der Graaff, W. N.; Tempelman, C. H.; Li, G.; Mezari, B.; Kosinov, N.; Pidko, E. A.; Hensen, E. J. Competitive Adsorption of Substrate and Solvent in Sn-Beta Zeolite During Sugar Isomerization. *ChemSusChem* **2016**, *9* (22), 3145−3149.
(44) Rai, N.; Caratzoulas, S.; Vlachos, D. G. Role of Silanol Group in Sn-Beta Zeolite for Glucose Isomerization and Epimerization Reactions. *ACS Catal.* **2013**, *3* (10), 2294−2298.
(45) Yang, G.; Pidko, E. A.; Hensen, E. J. M. The Mechanism of Glucose Isomerization to Fructose over Sn-BEA Zeolite: A Periodic Density Functional Theory Study. *ChemSusChem* **2013**, *6* (9), 1688−1696.
(46) Mushrif, S. H.; Varghese, J. J.; Krishnamurthy, C. B. Solvation dynamics and energetics of intramolecular hydride transfer reactions in biomass conversion. *Phys. Chem. Chem. Phys.* **2015**, *17* (7), 4961−4969.
(47) Vega-Vila, J. C.; Harris, J. W.; Gounder, R. Controlled insertion of tin atoms into zeolite framework vacancies and consequences for glucose isomerization catalysis. *J. Catal.* **2016**, *344*, 108−120.
(48) Chang, C. C.; Wang, Z. P.; Dornath, P.; Je Cho, H.; Fan, W. Rapid synthesis of Sn-Beta for the isomerization of cellulosic sugars. *RSC Adv.* **2012**, *2* (28), 10475−10477.
(49) Chen, N. Y. Hydrophobic Properties of Zeolites. *J. Phys. Chem.* **1976**, *80* (1), 60−64.
(50) Cybulskis, V. J.; Harris, J. W.; Zvinevich, Y.; Ribeiro, F. H.; Gounder, R. A transmission infrared cell design for temperature-controlled adsorption and reactivity studies on heterogeneous catalysts. *Rev. Sci. Instrum.* **2016**, *87* (10), 103101.
(51) Kresse, G.; Hafner, J. Ab-initio Molecular-Dynamics for Liquid-Metals. *Phys. Rev. B: Condens. Matter Mater. Phys.* **1993**, *47* (1), 558−561.
(52) Kresse, G.; Hafner, J. Ab-Initio Molecular-Dynamics Simulation of the Liquid-Metal Amorphous-Semiconductor Transition in Germanium. *Phys. Rev. B: Condens. Matter Mater. Phys.* **1994**, *49* (20), 14251−14269.
(53) Kresse, G.; Furthmüller, J. Efficient iterative schemes for ab initio total-energy calculations using a plane-wave basis set. *Phys. Rev. B: Condens. Matter Mater. Phys.* **1996**, *54* (16), 11169−11186.
(54) Kresse, G.; Furthmüller, J. Efficiency of ab-initio total energy calculations for metals and semiconductors using a plane-wave basis set. *Comput. Mater. Sci.* **1996**, *6* (1), 15−50.
(55) Blöchl, P. E. Projector augmented-wave method. *Phys. Rev. B: Condens. Matter Mater. Phys.* **1994**, *50* (24), 17953−17979.
(56) Kresse, G.; Joubert, D. From ultrasoft pseudopotentials to the projector augmented-wave method. *Phys. Rev. B: Condens. Matter Mater. Phys.* **1999**, *59* (3), 1758−1775.
(57) Perdew, J. P.; Burke, K.; Ernzerhof, M. Generalized Gradient Approximation Made Simple. *Phys. Rev. Lett.* **1996**, *77* (18), 3865−3868.
(58) Zhang, Y.; Yang, W. Comment on "Generalized Gradient Approximation Made Simple". *Phys. Rev. Lett.* **1998**, *80* (4), 890−890.
(59) Hammer, B.; Hansen, L. B.; Nørskov, J. K. Improved adsorption energetics within density-functional theory using revised Perdew-Burke-Ernzerhof functionals. *Phys. Rev. B: Condens. Matter Mater. Phys.* **1999**, *59* (11), 7413−7421.
(60) Grimme, S.; Antony, J.; Ehrlich, S.; Krieg, H. A consistent and accurate ab initio parametrization of density functional dispersion correction (DFT-D) for the 94 elements H-Pu. *J. Chem. Phys.* **2010**, *132* (15), 154104.
(61) Grimme, S.; Ehrlich, S.; Goerigk, L. Effect of the Damping Function in Dispersion Corrected Density Functional Theory. *J. Comput. Chem.* **2011**, *32* (7), 1456−1465.
(62) Monkhorst, H. J.; Pack, J. D. Special Points for Brillouin-Zone Integrations. *Phys. Rev. B* **1976**, *13* (12), 5188−5192.
(63) Jónsson, H.; Mills, G.; Jacobsen, K. W. Nudged elastic band method for finding minimum energy paths of transitions. In *Classical and Quantum Dynamics in Condensed Phase Simulations*; World Scientific: 2011; pp 385−404.
(64) Henkelman, G.; Jónsson, H. Improved tangent estimate in the nudged elastic band method for finding minimum energy paths and saddle points. *J. Chem. Phys.* **2000**, *113* (22), 9978−9985.
(65) Henkelman, G.; Jónsson, H. A dimer method for finding saddle points on high dimensional potential surfaces using only first derivatives. *J. Chem. Phys.* **1999**, *111* (15), 7010−7022.
(66) Baerlocher, C.; McCusker, L. B. Database of Zeolite Structures; http://www.iza-structure.org/databases/ (accessed 2018).
(67) Newsam, J. M.; Treacy, M. M. J.; Koetsier, W. T.; de Gruyter, C. B. Structural Characterization of Zeolite-Beta. *Proc. R. Soc. London, Ser. A* **1988**, *420* (1859), 375−405.
(68) Urakawa, A.; Bürgi, T.; Baiker, A. Sensitivity enhancement and dynamic behavior analysis by modulation excitation spectroscopy: Principle and application in heterogeneous catalysis. *Chem. Eng. Sci.* **2008**, *63* (20), 4902−4909.
(69) Bregante, D. T.; Priyadarshini, P.; Flaherty, D. W. Kinetic and spectroscopic evidence for reaction pathways and intermediates for olefin epoxidation on Nb in *BEA. *J. Catal.* **2017**, *348*, 75−89.
(70) Ressler, T. WinXAS: a program for X-ray absorption spectroscopy data analysis under MS-Windows. *J. Synchrotron Radiat.* **1998**, *5*, 118−122.
(71) Camblor, M. A.; Corma, A.; Valencia, S. Characterization of nanocrystalline zeolite Beta. *Microporous Mesoporous Mater.* **1998**, *25* (1−3), 59−74.
(72) Camblor, M. A.; Corma, A.; Mifsud, A.; PerezPariente, J.; Valencia, S. Synthesis of nanocrystalline zeolite Beta in the absence of alkali metal cations. In *Progress in Zeolite and Microporous Materials, Parts A−C*; Chon, H., Ihm, S. K., Uh, Y. S., Eds.; Elsevier Science Bv: Amsterdam, 1997; Vol. *105*, pp 341−348.
(73) Thornburg, N. E.; Thompson, A. B.; Notestein, J. M. Periodic Trends in Highly Dispersed Groups IV and V Supported Metal Oxide Catalysts for Alkene Epoxidation with H2O2. *ACS Catal.* **2015**, *5* (9), 5077−5088.
(74) Bonino, F.; Damin, A.; Bordiga, S.; Lamberti, C.; Zecchina, A. Interaction of CD3CN and Pyridine with the Ti(IV) Centers of TS-1 Catalysts: a Spectroscopic and Computational Study. *Langmuir* **2003**, *19* (6), 2155−2161.
(75) Eroshenko, V.; Regis, R. C.; Soulard, M.; Patarin, J. The heterogeneous systems 'water-hydrophobic zeolites': new molecular springs. *C. R. Phys.* **2002**, *3* (1), 111−119.
(76) Halasz, I.; Kim, S.; Marcus, B. Uncommon adsorption isotherm of methanol on a hydrophobic Y-zeolite. *J. Phys. Chem. B* **2001**, *105* (44), 10788−10796.

DOI: 10.1021/jacs.8b08336
J. Am. Chem. Soc. 2018, 140, 14244−14266

(77) Dose, M. E.; Zhang, K.; Thompson, J. A.; Leisen, J.; Chance, R. R.; Koros, W. J.; McCool, B. A.; Lively, R. P. Effect of Crystal Size on Framework Defects and Water Uptake in Fluoride Mediated Silicalite-1. *Chem. Mater.* **2014**, *26* (15), 4368−4376.
(78) Thiel, P. A.; Madey, T. E. The Interaction of Water with Solid-Surfaces - Fundamental-Aspects. *Surf. Sci. Rep.* **1987**, *7* (6−8), 211−385.
(79) Lercher, J. A.; Jentys, A. Infrared and Raman Spectroscopy for Characterizing Zeolites. In *Introduction to Zeolite Science and Practice*; Cejka, J., Bekkum, H. V., Corma, A., Schuth, F., Eds.; Elsevier Science Bv: Amsterdam, 2007; Vol. *168*, pp 435−476.
(80) Lawrence, C. P.; Skinner, J. L. Vibrational spectroscopy of HOD in liquid D2O. III. Spectral diffusion, and hydrogen-bonding and rotational dynamics. *J. Chem. Phys.* **2003**, *118* (1), 264−272.
(81) Eisenberg, D.; Kauzmann, W. *The Structure and Properties of Water*; OUP: Oxford, 2005.
(82) Bermejo-Deval, R.; Assary, R. S.; Nikolla, E.; Moliner, M.; Roman-Leshkov, Y.; Hwang, S. J.; Palsdottir, A.; Silverman, D.; Lobo, R. F.; Curtiss, L. A.; Davis, M. E. Metalloenzyme-like catalyzed isomerizations of sugars by Lewis acid zeolites. *Proc. Natl. Acad. Sci. U. S. A.* **2012**, *109* (25), 9727−9732.
(83) Li, Y. P.; Head-Gordon, M.; Bell, A. T. Analysis of the Reaction Mechanism and Catalytic Activity of Metal-Substituted Beta Zeolite for the Isomerization of Glucose to Fructose. *ACS Catal.* **2014**, *4* (5), 1537−1545.
(84) Roman-Leshkov, Y.; Moliner, M.; Labinger, J. A.; Davis, M. E. Mechanism of Glucose Isomerization Using a Solid Lewis Acid Catalyst in Water. *Angew. Chem., Int. Ed.* **2010**, *49* (47), 8954−8957.
(85) Gounder, R.; Davis, M. E. Titanium-Beta Zeolites Catalyze the Stereospecific Isomerization of D-Glucose to L-Sorbose via Intramolecular C5-C1 Hydride Shift. *ACS Catal.* **2013**, *3* (7), 1469−1476.
(86) Christianson, J. R.; Caratzoulas, S.; Vlachos, D. G. Computational Insight into the Effect of Sn-Beta Na Exchange and Solvent on Glucose Isomerization and Epimerization. *ACS Catal.* **2015**, *5* (9), 5256−5263.
(87) Wolf, P.; Valla, M.; Nunez-Zarur, F.; Comas-Vives, A.; Rossini, A. J.; Firth, C.; Kallas, H.; Lesage, A.; Emsley, L.; Copéret, C.; Hermans, I. Correlating Synthetic Methods, Morphology, Atomic-Level Structure, and Catalytic Activity of Sn-beta Catalysts. *ACS Catal.* **2016**, *6* (7), 4047−4063.
(88) Bermejo-Deval, R.; Gounder, R.; Davis, M. E. Framework and Extraframework Tin Sites in Zeolite Beta React Glucose Differently. *ACS Catal.* **2012**, *2* (12), 2705−2713.
(89) Madon, R. J.; Iglesia, E. Catalytic reaction rates in thermodynamically non-ideal systems. *J. Mol. Catal. A: Chem.* **2000**, *163* (1), 189−204.
(90) Miyajima, K.; Sawada, M.; Nakagaki, M. Studiess on Aqueous Solutions of Saccharides. 1. Activity Coefficients of Monosaccharides in Aqueous Solutions at 25 Degrees C. *Bull. Chem. Soc. Jpn.* **1983**, *56* (6), 1620−1623.
(91) Koretsky, M. *Engineering and Chemical Thermodynamics*; John Wiley & Sons, Inc.: Hoboken, NJ, 2004.
(92) Coblentz Society. Evaluated Infrared Reference Spectra. In *NIST Chemistry WebBook*; National Institute of Standards and Technology: Gaithersburg, MD, 2018.
(93) Hineno, M. Infrared Spectra and Normal Vibrations of Beta-D-Glucopyranose. *Carbohydr. Res.* **1977**, *56* (2), 219−227.
(94) Cael, J. J.; Koenig, J. L.; Blackwell, J. Infrared and Raman-Spectroscopy of Carbohydrates. Part 4. Identification of Configuration-Sensitive and Conformation-Sensitive Modes for D-Glucose by Normal Coordinate Analysis. *Carbohydr. Res.* **1974**, *32* (1), 79−91.
(95) Wells, H. A.; Atalla, R. H. An Investigation of the Vibrational Spectra of Glucose, Galactose and Mannose. *J. Mol. Struct.* **1990**, *224*, 385−424.
(96) Mathlouthi, M.; Vinh Luu, D. Laser-Raman Spectra of D-Glucose and Sucrose in Aqueous Solution. *Carbohydr. Res.* **1980**, *81* (2), 203−212.
(97) Ibrahim, M.; Alaam, M.; El-Haes, H.; Jalbout, A. F.; Leon, A. d. Analysis of the structure and vibrational spectra of glucose and fructose. *Ecletica Quim.* **2006**, *31*, 15−21.
(98) Bai, P.; Siepmann, J. I.; Deem, M. W. Adsorption of Glucose into Zeolite Beta from Aqueous Solution. *AIChE J.* **2013**, *59* (9), 3523−3529.
(99) Bare, S. R.; Kelly, S. D.; Sinkler, W.; Low, J. J.; Modica, F. S.; Valencia, S.; Corma, A.; Nemeth, L. T. Uniform Catalytic Site in Sn-Beta-Zeolite Determined Using X-ray Absorption Fine Structure. *J. Am. Chem. Soc.* **2005**, *127* (37), 12924−12932.
(100) Dijkmans, J.; Dusselier, M.; Janssens, W.; Trekels, M.; Vantomme, A.; Breynaert, E.; Kirschhock, C.; Sels, B. F. An Inner-/Outer-Sphere Stabilized Sn Active Site in beta-Zeolite: Spectroscopic Evidence and Kinetic Consequences. *ACS Catal.* **2016**, *6* (1), 31−46.
(101) Wolf, P.; Valla, M.; Rossini, A. J.; Comas-Vives, A.; Nunez-Zarur, F.; Malaman, B.; Lesage, A.; Emsley, L.; Coperet, C.; Hermans, I. NMR Signatures of the Active Sites in Sn-Beta Zeolite. *Angew. Chem., Int. Ed.* **2014**, *53* (38), 10179−10183.
(102) Liu, J. W.; Hibbitts, D.; Iglesia, E. Dense CO Adlayers as Enablers of CO Hydrogenation Turnovers on Ru Surfaces. *J. Am. Chem. Soc.* **2017**, *139* (34), 11789−11802.
(103) Chandler, D. Interfaces and the driving force of hydrophobic assembly. *Nature* **2005**, *437*, 640.
(104) Wilson, N. M.; Flaherty, D. W. Mechanism for the Direct Synthesis of H2O2 on Pd Clusters: Heterolytic Reaction Pathways at the Liquid−Solid Interface. *J. Am. Chem. Soc.* **2016**, *138* (2), 574−586.
(105) Kim, T. H.; Mehrabi, P.; Ren, Z.; Sljoka, A.; Ing, C.; Bezginov, A.; Ye, L. B.; Pomes, R.; Prosser, R. S.; Pai, E. F. The role of dimer asymmetry and protomer dynamics in enzyme catalysis. *Science* 2017, *355* (6322), DOI: 10.1126/science.aag2355.

DOI: 10.1021/jacs.8b08336
J. Am. Chem. Soc. 2018, 140, 14244−14266